WEAPONS CENTER LIBRARY

MCDONNELL DOUGLAS RESEARCH LABORATORIES

MCDONNELL DOUGLAS

CORPORATION

81 5 05 021

REPORT DOCUMENTATION PAGE	READ INSTRUCTIONS BEFORE COMPLETING FORM

1. REPORT NUMBER	2. GOVT ACCESSION NO. AD-A098513	3. RECIPIENT'S CATALOG NUMBER

4. TITLE *(and Subtitle)*	5. TYPE OF REPORT & PERIOD COVERED
LASER RADAR ANALYSES.	Final Report. 15 July 1979 — 15 July 1980
	6. PERFORMING ORG. REPORT NUMBER MDC-Q0714

7. AUTHOR(s)	8. CONTRACT OR GRANT NUMBER(s)
J. C. Leader	N60921-79-C-0180

9. PERFORMING ORGANIZATION NAME AND ADDRESS	10. PROGRAM ELEMENT, PROJECT, TASK AREA & WORK UNIT NUMBERS
McDonnell Douglas Research Laboratories McDonnell Douglas Corporation St. Louis, MO 63166	62332N; SF 32-399; SF 32 399 492 9F78EA

11. CONTROLLING OFFICE NAME AND ADDRESS	12. REPORT DATE
Naval Surface Weapons Center White Oak, Silver Spring, Maryland 20910 Attn: Code F46	15 July 1980
	13. NUMBER OF PAGES 75

14. MONITORING AGENCY NAME & ADDRESS *(if different from Controlling Office)*	15. SECURITY CLASS. *(of this report)*
F32399	Unclassified
	15a. DECLASSIFICATION/DOWNGRADING SCHEDULE

16. DISTRIBUTION STATEMENT *(of this Report)*

Approved for public release; distribution unlimited

17. DISTRIBUTION STATEMENT *(of the abstract entered in Block 20, if different from Report)*

DTIC ELECTE MAY 5 1981 S C

18. SUPPLEMENTARY NOTES

19. KEY WORDS *(Continue on reverse side if necessary and identify by block number)*

Laser radar
Heterodyne
Speckle
Atmospheric turbulence

Cross section
Target signature
Glint

20. ABSTRACT *(Continue on reverse side if necessary and identify by block number)*

General integral expressions for the power signal and power signal-to-noise ratio arising from laser heterodyne detection of a distorted optical phase front are derived. Specific analytical results for the efficiency of heterodyne detection are derived for a generalized transceiver system that include the effects of local oscillator and receiver aperture size and focal lengths as well as the amplitude radius of the Gaussian local oscillator. Efficiency effects are calculated assuming the phase front distortions arise

DD FORM 1473 EDITION OF 1 NOV 65 IS OBSOLETE

405315

from target scattering of a laser signal (speckle effects) and scintillation resulting from atmospheric turbulence. Specific numerical calculations of the signal-to-noise ratio efficiency illustrate the degradation in signal-to-noise ratio resulting from diffuse scattering from extended targets at close range and atmospheric turbulence effects at long range. These calculations indicate the requirement for a minimum receiving aperture size (commensurate with total received signal requirements) and a uniform local oscillator beam that underfills the target image (on the photocathode) for optimum laser radar efficiency.
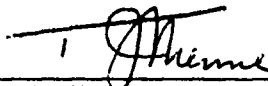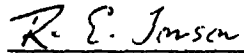
FOREWORD

This report is an account of the work performed at the McDonnell Douglas Research Laboratories on Laser Radar Analyses for the Naval Surface Weapons Center, Contract No. N60921-79-C-0180, from 15 July 1979 to 15 July 1980. The work was performed in the Radiation Sciences Department, managed by Dr. T. J. Menne. The principal investigator was Dr. J. C. Leader. The project monitor was Dr. R. E. Jensen, Naval Surface Weapons Center.

This technical report has been reviewed and is approved.

T. J. Menne
Chief Scientist, Radiation Sciences
McDonnell Douglas Research Laboratories

D. P. Ames
Staff Vice President
McDonnell Douglas Research Laboratories

R. E. Jensen
Project Monitor
Naval Surface Weapons Center

Accession For	
NTIS GRA&I	✓
DTIC TAB	☐
Unannounced	☐
Justification	
By	
Distribution/	
Availability Codes	
	Avail and/or
Dist	Special
A	

TABLE OF CONTENTS

LIST OF ILLUSTRATIONS

LIST OF ILLUSTRATIONS

LIST OF ILLUSTRATIONS

LIST OF TABLES

1. INTRODUCTION

Coherent laser detection and ranging (LADAR) systems are currently being developed for the acquisition and tracking of extended targets. Although heterodyne detection of the optical signal generally provides significant signal-to-noise ratio enhancement over incoherent detection for infrared wavelengths, the average signal (and resultant signal-to-noise ratio) may be significantly degraded by phase-front distortion resulting from target speckle and atmospheric turbulence effects unless proper system design precautions are observed. Similarly, monopulse tracking performance of LADAR systems can be degraded unless phase-distortion effects are understood and compensated. The objective of this study is to develop analyses and computer codes that permit reliable predictions of phase-distortion effects on heterodyne LADAR performance for realistic system parameters, target configurations, and engagement scenarios. This final report summarizes the results that have been obtained through 15 July 1980 concerning the efficiency of the heterodyne-detection process resulting solely from extra-instrumental phase effects (i.e., unavoidable instrument inefficiencies are neglected).

1

2. SUMMARY OF RESULTS

Significant results of the contract study are summarized below. Detailed analytical results are provided in Section 5, and illustrative numerical results are given in Section 6.

- A general integral expression was derived relating the average efficiency of heterodyne detection to the degree of coherence function, characterizing the spatial phase variations, at the entrance pupil of a generalized laser transceiver system.

- Specific integral expressions were derived for the heterodyne efficiency of a transceiver having arbitrary entrance-pupil radius, receiver focal length, local oscillator aperture, and local oscillator Gaussian amplitude distribution and focal length in response to a Schell-model source propagating through atmospheric turbulence and an arbitrary target laser-reflectance distribution viewed through atmospheric turbulence.

- Computer codes were developed that evaluate the laser heterodyne efficiency for both Schell-model sources and general target reflectance functions.

- Computer codes were developed that calculate projected laser radar cross-section distributions for both spherical and conical targets having arbitrary (homogeneous) surface-roughness characteristics.

- Heterodyne-detection efficiencies were calculated for representative transceiver and target parameters. These calculations provide specific functional relations for the increase in heterodyne efficiency with increasing target range, decreasing target size, and decreasing receiver entrance pupil along with other desired functional relations involving other transceiver parameters and target characteristics.

3. CONCLUSIONS

Salient conclusions resulting from this study are summarized below.

- Heterodyne-detection inefficiency resulting from target-induced laser speckle can significantly degrade LADAR performance for close ranges (~ 1 km) and fully illuminated target conditions unless small aperture receivers (on the order of a speckle cell diameter) are employed. Inefficiencies of 15 dB or greater can result at close range.

- Atmospheric scintillation does not significantly degrade heterodyne-detection efficiency for target ranges up to 10 km at a 10.6 μm laser wavelength. A 5 dB degradation in signal-to-noise ratio is the maximum effect expected for an extended target at 10 km range.

- Smooth targets generally provide a higher signal-to-noise ratio for heterodyne detection than corresponding rough targets because of the greater spatial coherence at the receiver.

- A uniform local-oscillator beam (such as obtained from an apertured TEM_{00} laser beam) that encloses a slightly smaller area on the photodetector than the target image is required for optimum heterodyne detection efficiency.

4. RECOMMENDATIONS

- The receiving apertures used for heterodyne detection of laser radar signals should be designed such that the spatial extent of the aperture is minimized consonant with requirements for total received signal. A circular receiving aperture (non-Cassegrainian) is optimum for minimizing speckle-induced heterodyne inefficiencies resulting from laser scattering from a symmetric diffuse target.

- Laser radar transceivers should be designed so that the local oscillator beam is approximately uniform and encloses an area on the photodetector within the target image.

- Experiments should be performed to measure the efficiency of laser heterodyne detection for a variety of target and receiver configurations that conform to the analytical assumptions used in this study. A detailed comparison between measured and calculated results should be performed to determine the degree of validity of the analyses and any inefficiency effects requiring further investigation.

- The anlytical techniques developed in this study should be extended to treat the sum and difference signals arising from two heterodyne detectors in the focal plane of a receiver system, simulating the tracking signal arising from a monopulse LADAR. Numerical computations of the resultant expressions should determine the magnitude of the tracking-error signal arising from speckle and scintillation effects.

5. ANALYSES

Analytical results obtained under the contract study are presented below. Section 5.1 provides the basic heterodyne-efficiency derivation, while Sections 5.2 and 5.3 respectively treat the efficiency resulting from a Schell-model source and a generalized laser radar cross-section distribution. Section 5.4 summarizes the treatment of target reflectivities.

5.1 Laser Heterodyne-Detection Efficiency

This section provides an analysis of the average efficiency of heterodyne detection for a generalized transceiver system in response to a phase front that is distorted by diffuse scattering from the target (speckle) and atmospheric turbulence. Because each pulse detected by the transceiver represents one sample of statistically equivalent configurations of the target and the atmosphere, the average efficiency is treated by considering the phase-front correlations (i.e., the mutual intensity function) that result from an average over the ensemble of possible configurations. In practice, wind and target motions provide a temporal succession of pulse samples such that a time average closely approximates the assumed ensemble average. Utilizing the development of Reference 1, the ensemble-averaged photodetector current correlation function of a heterodyne LADAR system can be expressed as

$$\left\langle x_{IF}(t)\, x_{IF}(t-\tau) \right\rangle = \frac{2\alpha^2}{z_o^2} \operatorname{Re} \iiiint\limits_{\substack{\text{detector} \\ \text{area}}} d^2\vec{r}\, d^2\vec{r}'\; \Gamma(\vec{r},\vec{r}',\tau)\; U_\ell(\vec{r}) U_\ell^*(\vec{r}')\, e^{i\omega_{IF}\tau}\, \mathscr{G}(t)\mathscr{G}(t-\tau),$$

(1)

where

x_{IF} = heterodyne intermediate-frequency photocurrent

Γ = scalar mutual coherence function incident on photodetector

t = time

$\vec{r}$ = transverse coordinate across photodetector surface

U_ℓ = local oscillator field

$\mathscr{G}(t)$ = pulse shape

ω_{IF} = Doppler-shifted heterodyne frequency

$$\tau \quad = t - t'$$

$$\alpha \quad = \eta Ge/2h\nu$$

$\eta \quad$ = detector quantum efficiency

$G \quad$ = gain

$e \quad$ = electronic charge

$h \quad$ = Planck's constant

$z_0 \quad$ = free-space impedence

$\nu \quad$ = photon frequency.

Equation (1) is identical to Equation (15) of Reference 1 except that one component of the field is considered (hence the scalar form of the general vector expression is employed) and the temporal pulse form has been separated from the target/atmosphere-dependent mutual coherence function. Noting that the current power spectral density $S(\nu)$ and the current correlation function are related by the Fourier transform pairs,

$$S(\nu) = \int_{-\infty}^{\infty} d\tau \, e^{-i2\pi\nu\tau} \left\langle x_{IF}(t) \, x_{IF}(t - \tau) \right\rangle, \tag{2a}$$

and

$$\left\langle x_{IF}(t) \, x_{IF}(t - \tau) \right\rangle = \int_{-\infty}^{\infty} d\nu \, e^{i2\pi\nu\tau} S(\nu), \tag{2b}$$

it is clear that the ensemble-averaged current power, S^T, integrated over the (relatively small) frequency bandwidth resulting from current fluctuations is given by

$$S^T = \int_{-\infty}^{\infty} d\nu \, S(\nu) = \left\langle x_{IF}(t) \, x_{IF}(t) \right\rangle. \tag{3}$$

Thus, the frequency-integrated, ensemble-averaged current power depends only on the current variance. Therefore, the temporal variable τ can be eliminated from further consideration in the evaluation of S^T with the understanding that

the function Γ is defined only when the pulse is "on." The mutual coherence function evaluated for zero time delay ($\tau = 0$) is known as the mutual intensity function (MIF) and will be referred to as such in the ensuing analysis.

It is convenient for the purposes of subsequent analyses to define the interference integral of Equation (1) in a plane (having transverse coordinate $\vec{\xi}$) located in front of the receiving aperture. Denoting by $U_{\ell b}(\vec{\xi})$ the local oscillator field amplitude back-propagated from the photodetector to the receiving aperture plane, the average frequency integrated current power is

$$S^T = \frac{2\alpha^2}{z_o^2} \iiiint_{A_{bp}} d^2\xi\, d^2\xi'\; \Gamma(\vec{\xi},\vec{\xi}')\; U_{\ell b}(\vec{\xi})\; U_{\ell b}^*(\vec{\xi}'), \tag{4}$$

where A_{bp} is the back-propagated aperture area (i.e., the minimum areal subtense of either the receiving aperture or the back-propagated local-oscillator wave, whichever is less). Equivalently, Equation (4) can be written

$$S^T = \frac{2\alpha^2}{z_o^2}\, U_o^2\, U_{\ell b}^2 \iiiint_{A_{bp}} d^2\xi\, d^2\xi'\; \gamma(\vec{\xi},\vec{\xi}')\; u_{\ell b}(\vec{\xi})\; u_{\ell b}^*(\vec{\xi}'), \tag{5}$$

where $u_{\ell b}$ is the normalized spatial variation of the back-propagated local oscillator wave and $U_{\ell b}$ is the magnitude, viz.,

$$U_{\ell b}(\vec{\xi}) = U_{\ell b}\, u_{\ell b}(\vec{\xi}), \tag{6}$$

where $|u_{\ell b}(\xi)|_{max} = 1$, and $\gamma(\vec{\xi},\vec{\xi}')$ is the corresponding normalized MIF, viz.,

$$\Gamma(\vec{\xi},\vec{\xi}') = U_o^2\, \gamma(\vec{\xi},\vec{\xi}'), \tag{7}$$

where $|\gamma(\vec{\xi},\vec{\xi}')|_{max} = 1$. When the average intensity [i.e., $\langle U(\vec{\xi})\, U*(\vec{\xi})\rangle = \Gamma(\vec{\xi},\vec{\xi}')$] is approximately constant over the receiver aperture (true for most cases of interest), $\gamma(\vec{\xi},\vec{\xi}')$ is the spatial degree of coherence function.

Assuming shot-noise-limited detection, the frequency-integrated current noise power is[1]

$$N^T = \int_{-\infty}^{\infty} S_{shot}(\nu)d\nu = \int_{\nu_1}^{\nu_2} G^2\, 2e\, \frac{x_{DC}}{G}\, d\nu = 2e\, x_{DC}\, G\Delta\nu \,, \tag{8}$$

where x_{DC} is the direct current level and $\Delta\nu$ is the bandwidth. The direct current level results from the local oscillator power level[1], and hence the noise power can be written as

$$N^T = 2eG\Delta\nu \times 2\alpha\, P_\ell = \frac{2eG\alpha\Delta\nu}{z_o}\, U_{\ell b}^2 \iint\limits_{A_{bp}} d^2\vec{\xi}\, |u_{\ell b}(\vec{\xi})|^2 \,. \tag{9}$$

Thus, the average current power signal-to-noise ratio is given by

$$\frac{S^T}{N^T} = \frac{\eta\, U_o^2}{2h\nu z_o \Delta\nu}\, \frac{\displaystyle\iiiint\limits_{A_{bp}} d^2\vec{\xi}\, d^2\vec{\xi}'\, \gamma(\vec{\xi},\vec{\xi}')\, u_{\ell b}(\vec{\xi})\, u_{\ell b}^*(\vec{\xi}')}{\displaystyle\iint\limits_{A_{bp}} d^2\vec{\xi}\, |u_{\ell b}(\vec{\xi})|^2} \,. \tag{10}$$

Clearly, optimal signal-to-noise ratios are achieved when the incident field replicates the spatial distribution of the local oscillator field, i.e.,

$$\gamma(\vec{\xi},\vec{\xi}') = u_{\ell b}(\vec{\xi})\, u_{\ell b}^*(\vec{\xi}') \,, \tag{11}$$

yielding the ideal signal-to-noise ratio

$$\left.\frac{S^T}{N^T}\right|_{\substack{ideal \\ \ell.o.}} = \frac{\eta\, ?_s^1}{h\nu\Delta\nu} \,, \tag{12}$$

where

$$P_s^i = \frac{U_o^2}{2 z_o} \iint\limits_{A_r} d^2\xi' \ |u_{\ell b}(\vec{\xi}')|^2 \tag{13}$$

is the received signal power for a perfectly phase-matched incident signal in the receiving aperture encompassing the area A_r. In general, however, the phase fluctuations occurring in the incident field preclude obtaining the ideal (maximum) signal-to-noise ratio so that the actual ratio achieved as a result of the spatial phase fluctuations can be expressed as

$$\frac{S^T}{N^T} = \frac{P_s \ \eta}{h\nu\Delta\eta} \ \epsilon_{\ell.o.}, \tag{14}$$

where $\epsilon_{\ell.o.}$ is the local oscillator efficiency factor defined as

$$\epsilon_{\ell.o.} = \frac{S^T}{N^T} \left(\frac{S^T}{N^T} \Bigg|_{\substack{ideal \\ \ell.o.}} \right)^{-1} = \frac{\iiiint\limits_{A_{bp}} d^2\xi d^2\xi' \gamma(\vec{\xi},\vec{\xi}') \ u_{\ell b}(\vec{\xi}) \ u_{\ell b}^*(\vec{\xi}')}{\iint\limits_{A_{bp}} d^2\xi \ |u_{\ell b}(\vec{\xi})|^2 \ \iint\limits_{A_r} d^2\xi' \ |u_{\ell b}(\vec{\xi}')|^2}. \tag{15}$$

Although Equation (15) provides a valid representation of the local-oscillator efficiency, it is often more appropriate for LADAR analyses to consider the maximum signal-to-noise ratio that is achievable from the total power enclosed by the receiving aperture, i.e.,

$$\frac{S^T}{N^T}\Bigg|_{max} = \frac{\eta \ P_s^m}{h\nu\Delta\nu}, \tag{16}$$

where

$$P_s^m = \frac{U_o^2}{2 z_o} \iint\limits_{A_r} d^2\xi' = \frac{U_o^2}{2 z_o} A_r, \tag{17}$$

and it is again assumed that the received intensity is constant over the receiving aperture. In this case the maximum power signal-to-noise ratio heterodyne efficiency factor is given by

$$\varepsilon_{max} = \frac{S^T}{N^T} \left(\frac{S^T}{N^T}\bigg|_{max}\right)^{-1} = \frac{\displaystyle\iiiint_{A_{bp}} d^2\xi\, d^2\xi'\; \gamma(\vec{\xi},\vec{\xi}')\, u_{\ell b}(\vec{\xi})\, u^*_{\ell b}(\vec{\xi}')}{A_r \displaystyle\iint_{A_{bp}} d^2\xi\, |u_{\ell b}(\vec{\xi})|^2}. \tag{18}$$

5.2 Schell-Model Source Efficiency Factors

To permit specific calculations of LADAR efficiency factors, the generalized transceiver system depicted in Figure 1 is considered and a Schell-model source is assumed for the ensuing development. The parameters of the Figure 1 transceiver are as follows:

A = local oscillator aperture radius,

P = entrance pupil radius,

f_ℓ = focal length of local oscillator lens/mirror (lens 3), and

f_r = focal length of receiving lens/mirror (lens 2).
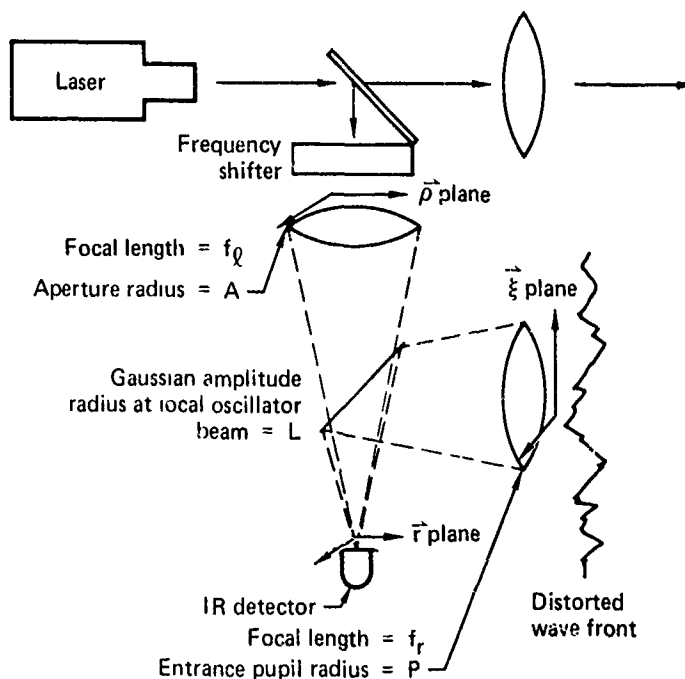
GP03-0639-1

Figure 1. Transceiver parameters and coordinates.

A TEM$_{00}$ mode local oscillator beam is assumed such that the (scalar) local oscillator amplitude is given by

$$U_{\ell o}(\vec{\rho}) = |U_{\ell o}| \; e^{-|\vec{\rho}|^2/L_o^2} \tag{19}$$

in the plane (having transverse coordinates $\vec{\rho}$) located in front of lens 3.

Because a Schell-model source is assumed,[2] the incident mutual intensity function can be expressed as

$$\Gamma_s(\vec{\xi},\vec{\xi}') = U_o^2 \; e^{-\frac{k}{2}(\alpha|\vec{\xi}|^2 + \alpha*|\xi'|^2)} \; e^{-|\vec{\xi}-\vec{\xi}'|^2/r_c^2} \;, \tag{20}$$

where r_c is the coherence radius and

$$\alpha = \frac{2}{kL_A} + \frac{1}{L_\phi} \;, \tag{21}$$

where L_A is the amplitude radius and L_ϕ is the average phase-front radius of curvature.

Utilizing the Fresnel diffraction integral, the local oscillator field amplitude in the photo-detector plane is given by

$$U_{\ell o}(\vec{r}) = \frac{U_{\ell o} \; e^{\frac{ik}{2f_\ell}\vec{r}^2}}{(i\lambda f_\ell)} \int\!\!\!\int_{-\infty}^{\infty} d^2\vec{\rho} \; P(\vec{\rho}) \; e^{-\frac{\rho^2}{L_o^2}} \; e^{-\frac{ik}{f_\ell}\vec{r}\cdot\vec{\rho}} \;, \tag{22}$$

where

$$P(\vec{\rho}) = \begin{cases} 1 & \text{when } \vec{\rho}^2 < A^2 \\ 0 & \text{when } \vec{\rho}^2 > A^2 \end{cases} \tag{23}$$

is the local-oscillator-pupil function. Similarly, the photo-detector field is related to the back-propagated local-oscillator field by the expression

$$U_{\ell o}(\vec{r}) = \frac{e^{\frac{ik}{2f_r}\vec{r}^2}}{(i\lambda f_r)} \iint\limits_{-\infty}^{\infty} d^2\vec{\xi} \; U_{\ell b}(\vec{\xi}) \; e^{-\frac{ik}{f_r}\vec{\xi}\cdot\vec{r}} \quad . \tag{24}$$

Hence, the back-propagated field can be expressed as

$$U_{\ell b}(\vec{\xi}) = \frac{k^2}{f_r f_\ell} \iint\limits_{-\infty}^{\infty} d^2\vec{r} \; e^{\frac{ik}{f_r}\vec{\xi}\cdot\vec{r}} \; H(\vec{r}) \; G(\vec{r}) \quad , \tag{25}$$

where

$$H(\vec{r}) = e^{\frac{ik\vec{r}^2}{2}\left(\frac{1}{f_\ell} - \frac{1}{f_r}\right)} \tag{26}$$

and

$$G(\vec{r}) = U_{\ell o} \iint\limits_{-\infty}^{\infty} d^2\vec{\rho} \; P(\vec{\rho}) \; e^{-\frac{\rho^2}{L_o^2}} e^{-\frac{ik}{f_\ell}\vec{r}\cdot\vec{\rho}} \tag{27}$$

utilizing the inverse Fourier transform of Equation (24). Equation (25) can be expressed in convolution form, i.e.,

$$U_{\ell b}(\vec{\xi}) = \frac{k^2}{f_r f_\ell} \left(\frac{k}{f_r}\right)^2 \iint\limits_{-\infty}^{\infty} d^2\vec{\xi}' \; \tilde{H}(\vec{\xi} - \vec{\xi}') \; \tilde{G}(\vec{\xi}') \quad , \tag{28}$$

12

where

$$\tilde{H}(\vec{\xi}) = \iint\limits_{-\infty}^{\infty} d^2\vec{r}\ e^{\frac{ik}{f_r}\vec{\xi}\cdot\vec{r}}\ H(\vec{r}) = \frac{\pi}{iz}\ e^{-\frac{\vec{\xi}^2 k^2}{4f_r^2 iz}}, \qquad (29)$$

$$z = \frac{k}{2}\left(\frac{1}{f_\ell} - \frac{1}{f_r}\right), \qquad (30)$$

and

$$\tilde{G}(\vec{\xi}) = \iint\limits_{-\infty}^{\infty} d^2\vec{r}\ e^{\frac{ik}{f_r}\vec{\xi}\cdot\vec{r}}\ G(\vec{r}) = \left(\frac{f_\ell}{k}\right)^2 P\left(\vec{\xi}\frac{f_\ell}{f_r}\right) e^{-\frac{\xi^2}{L_o^2}\frac{f_\ell^2}{f_r^2}} U_{\ell o}. \qquad (31)$$

Thus, the back-propagated local-oscillator field is given by

$$U_{\ell b}(\vec{\xi}) = \frac{\pi}{iz}\frac{k^2 f_\ell}{f_r^3} U_{\ell o} \iint\limits_{-\infty}^{\infty} d^2\vec{\xi}'\ e^{-\frac{(\vec{\xi}-\vec{\xi}')^2 k^2}{4 f_r^2 iz}} e^{-\frac{\xi'^2}{L_o^2}\frac{f_\ell^2}{f_r^2}} \theta(A^2 f_r^2/f_\ell^2 - \xi'^2),$$

$$(32)$$

where $\theta(x)$ is the Heaviside function.

The integral form of Equation (32) is not analytically integrable because of the finite range imposed by the Heaviside function. If it is assumed that the aperture area goes to infinity, Equation (32) is easily evaluated, yielding

$$U_{\ell b}(\vec{\xi}) \xrightarrow[A\to\infty]{} \frac{\pi^2}{z'} \left(\frac{f_\ell}{f_r}\right) e^{i\xi^2/4z'} \, U_{\ell o}\left(\frac{1}{4z'} + iL'^{-2}\right)^{-1} \exp\left[-\xi^2\left(-4iz' + 16z'^2 L'^{-2}\right)^{-1}\right],$$

$$(33)$$

where

$$z' = z\,\frac{f_r^2}{k^2} \tag{34}$$

and

$$L'^{-2} = \frac{f_\ell^2}{f_r^2} L_o^{-2}. \tag{35}$$

A result that is identical to Equation (33) is obtained if Equation (32) is evaluated by the method of double stationary phase,[3] providing the stationary phase point, given by

$$\xi'_o = \xi\,\frac{(1 - 4iz'L'^{-2})}{1 + (4z'L'^{-2})^2}, \tag{36}$$

lies within the domain of integration. Because of the high frequencies associated with LADAR systems, the factor $z'L'^{-2}$ appearing in Equation (36) is much less than unity (it is zero for matched focal lengths, i.e., $f_\ell = f_r$) and thus $\xi'_o \approx \xi$. Because the stationary phase result equals the infinite limit result [Equation (33)], the major contribution to the integral arises from the domain of integration in the immediate neighborhood of the stationary phase point. Therefore, the integral of Equation (32) is approximately given by

$$U_{\ell b}(\vec{\xi}) \approx U_{\ell o}\,\frac{\pi^2}{z'} \left(\frac{f_\ell}{f_r}\right) e^{i\xi^2/4z'}\left(\frac{1}{4z'} + iL'^{-2}\right)^{-1} \exp\left[-\xi^2\left(-4iz' + 16z'\,L'^{-2}\right)^{-1}\right]$$

$$\theta\left(A^2\,\frac{f_r^2}{f_\ell^2} - \xi^2\right). \tag{37}$$

Utilizing the Equation (37) result for the back-propagated local-oscillator wave, the signal power, Equation (5), can be expressed as

$$S^T \sim U_o{}^2 \, |K|^2 \iiiint\limits_{-\infty}^{\infty} d^2\vec{\xi}\, d^2\vec{\xi}\,' \; \exp\left[-\vec{\xi}\,^2\left(\beta + \alpha\,\frac{k}{2}\right) - \vec{\xi}\,'^2\left(\beta^* + \alpha^*\,\frac{k}{2}\right) - |\vec{\xi} - \vec{\xi}\,'|^2 r_c{}^{-2}\right]$$

$$\times\, \theta\!\left(A'^{-2} - \vec{\xi}\,^2\right)\cdot \theta\!\left(A'^{-2} - \vec{\xi}\,'^2\right)\, \theta\!\left(P^2 - \vec{\xi}\,^2\right)\, \theta\!\left(P^2 - \vec{\xi}\,'^2\right), \tag{38}$$

where

$$K = \frac{\pi^2}{z'}\left(\frac{f_\ell}{f_r}\right)\left(\frac{1}{4z'} + iL'^{-2}\right)^{-1} U_{\ell o}, \tag{39}$$

$$\beta = \frac{-1}{4z'} + \left(-4iz' + 16z'^2 L'^{-2}\right)^{-1}, \tag{40}$$

$$A' = A\, f_r / f_\ell, \tag{41}$$

and the Schell-model source of Equation (20) is assumed. Equation (38) can be written in more compact form, viz.,

$$S^T \sim U_o{}^2 |K|^2 \iiiint\limits_{-\infty}^{\infty} d^2\vec{\xi}\, d^2\vec{\xi}\,' \; e^{-\alpha_o \vec{\xi}\,^2 - \alpha_o^* \vec{\xi}\,'^2 + 2r_c{}^{-2}\vec{\xi}\cdot\vec{\xi}\,'}$$

$$\times\, \theta\!\left(R_m{}^2 - \vec{\xi}\,^2\right)\, \theta\!\left(R_m{}^2 - \vec{\xi}\,'^2\right), \tag{42}$$

where

$$\alpha_o = \beta + \frac{k}{2}\,\alpha + r_c{}^{-2} \tag{43}$$

and

$$R_m = \begin{cases} A' & \text{if } A' < P \\ P & \text{if } P < A' \end{cases} \tag{44}$$

utilizing the properties of the Heaviside function. Equation (42) can now be
approximately integrated utilizing the double stationary-phase method yielding

$$s^T \approx \frac{\pi^2 U_o^2 |K|^2}{(\alpha_o \alpha_o^* - r_c^{-4})} Re \left\{ 1 - \exp\left[- R_m^2 \left(\alpha_o - (r_c^4 \alpha_o^*)^{-1} \right) \right] \right\} . \tag{45}$$

The parameters of many problems of interest, however, invalidate the
stationary-phase result of Equation (45) (see Section 6), so that in many
cases numerical integration techniques must be employed. A transformation to
polar coordinates permits analytical integration over the angular variables so
that Equation (42) can be reduced to a two-fold integral of the form

$$s^T = U_o^2 |K|^2 (2\pi)^2 \int_o^{R_m} \int_o^{R_m} d\xi d\xi' \xi\xi' I_o\left(\frac{2\xi\xi'}{r_c^2}\right) e^{-\alpha_o \xi^2 - \alpha_o^{*2} \xi'^2} , \tag{46}$$

where I_o is the zeroth-order modified Bessel function of the first kind. The
finite integrals of Equation (46) can be integrated by standard numerical
methods. The integral result of Equation (46) can be combined with the
relatively straightforward integration of the required local oscillator
intensities, using the back-propagated wave result [Equation (37)], to obtain
the following specific functional forms for the local-oscillator efficiency
[Equation (15)] and maximum heterodyne efficiency [Equation (18)]:

$$\varepsilon_{\ell.o.} = 4(\beta + \beta^*)^2 \left(1 - e^{-(\beta+\beta^*)R_m^2} \right)^{-1} \left(1 - e^{-(\beta+\beta^*)P^2} \right)^{-1}$$

$$\tag{47}$$

$$\times \int_o^{R_m} \int_o^{R_m} d\xi d\xi' \xi\xi' I_o\left(\frac{2\xi\xi'}{r_c^2}\right) e^{-\alpha_o \xi^2 - \alpha_o^* \xi'^2}$$

and

16

$$\varepsilon_{max} = 4(\beta + \beta*)P^{-2} \left(1 - e^{-(\beta+\beta*)R_m^2}\right)^{-1}$$

(48)

$$\times \int_0^{R_m} \int_0^{R_m} d\xi\, d\xi'\, \xi\xi'\, I_0\left(\frac{2\xi\xi'}{r_c^2}\right) e^{-\alpha_0\xi^2 - \alpha_0*\xi'^2} .$$

5.3 Heterodyne Detection Efficiency for General LRCS Distributions

The vacuum, far-field, mutual intensity function resulting from incoherent laser scattering from a rough object can be written[4]

$$\Gamma_{inc}^{vac}(\vec{\xi}^+, \vec{\xi}^-) \sim e^{-\frac{ik}{R}\vec{\xi}^+, \vec{\xi}^-} \int\int_{-\infty}^{\infty} d^2\vec{p}\, e^{-\frac{ik}{R}\vec{p}\cdot\vec{\xi}^-} \frac{d^2\sigma(\vec{p})}{d\vec{p}^2} ,$$

(49)

where

$$\vec{\xi}^+ = \frac{1}{2}(\vec{\xi} + \vec{\xi}') ,$$

$$\vec{\xi}^- = \vec{\xi} - \vec{\xi}' ,$$

$$R = \text{range to target} ,$$

$$\vec{p} = \text{transverse coordinate to line-of-sight at the target plane} ,$$

and

$$\frac{d^2\sigma(\vec{p})}{d\vec{p}^2} = \text{differential projected scattering cross-section per unit area.}$$

Equation (49) replicates Equation (1) of Reference 1 except for constant factors, the conversion of angle coordinates to linear displacements, and the rewriting of the range difference factor in terms of sum and difference

17

coordinates (i.e., $R - R' = \vec{\xi}^+ \cdot \vec{\xi}^-/R$). Although the Equation (49) prescription for the MIF is valid only in the far-field, the Reference 5 development demonstrates that this range is much smaller than the classic far-field range (on the order of the body dimensionality) for relatively incoherent scatterers. Reference 6 demonstrates that atmospheric turbulence modifies the vacuum MIF in the following manner:

$$\Gamma^{turb}(\vec{P}^+, \vec{P}^-) = \frac{\cos^2\theta^+}{(2\pi)^2} \iint\limits_{-\infty}^{\infty} d^2\hat{\zeta} \frac{\Gamma^{vac}(R\hat{\zeta},\vec{P}^-)}{(1 - \zeta_x^2 - \zeta_y^2)} \hat{F}(\hat{s}^+ - \hat{\zeta}, \vec{P}^-) , \qquad (50)$$

where $\hat{\zeta}$ and $\hat{s}^+$ are unit pointing vectors and $\hat{F}$ is the Fourier-transformed two-source, spherical-wave, atmospheric MIF. Because the integral of Equation (49) is functionally independent of the average field-point coordinate, $\vec{\xi}^+$, the integrated functional form for the vacuum MIF in Equation (50) is that of the exponential multiplying the integral of Equation (49), which is the functional description of a spherical phase front. Thus, the MIF that describes the field correlations resulting from incoherently scattered laser radiation propagating through atmospheric turbulence is of the form

$$\Gamma^{turb}_{inc} \sim e^{-\xi^{-2}/\rho_o^2} e^{-ik R^{-1} \vec{\xi}^+ \cdot \vec{\xi}^-} \iint\limits_{-\infty}^{\infty} d^2\vec{p}\, e^{-\frac{ik}{R} \vec{p} \cdot \vec{\xi}^-} \frac{d^2\sigma(\vec{p})}{d\vec{p}^2} , \qquad (51)$$

where $\rho_o = [3/8 \times 1.455\, k^2 R C_n^2]^{-3/5}$ is the spherical wave coherence length.[6]

Glint points on the surface of an object scatter radiation in the form of spherical waves with a scattering cross section (in the geometrical optics approximation) given by π times the product of the Gaussian radii of curvature. Thus, assuming (for the purposes of subsequent analyses) a rough object having one centrally located glint point, the degree of coherence function will be given by

$$\gamma(\vec{\xi}^+, \vec{\xi}^-) = e^{-ik\ R^{-1}\ \vec{\xi}^+\cdot\vec{\xi}^-}\ e^{-\xi^{-2}/\rho_o}\left[\pi a_1\ a_2 + \Lambda \iint\limits_{-\infty}^{\infty} d^2\vec{p}\ e^{\frac{ik}{R}\ \vec{p}\cdot\vec{\xi}^-}\ \frac{d^2\sigma(\vec{p})}{d\vec{p}^2}\right]$$

(52)

$$\times\left[1 + \Lambda \iint\limits_{-\infty}^{\infty} d^2\vec{p}\ \frac{d^2\sigma(\vec{p})}{i\vec{p}^2}\right]^{-1},$$

where a_1 and a_2 are the Gaussian radii of curvature at the glint point, Λ is a factor that relates the relative strength of the coherent (glint) and incoherent components, and the denominator of Equation (52) results from the normalization requirement of the degree-of-coherence function. Reference 7 demonstrates that the coherent component of surface scattering is attenuated by an exponential factor of the form $e^{-\sigma_\phi^2}$ where σ_ϕ represents the phase variance and can be related to the rough-surface height deviation. Reference 8 shows that rough-surface speckle statistics are replicated when the incoherent component of the MIF is attenuated as the phase deviation decreases according to the factor $(1 - e^{-\sigma_\phi^2})$. Thus, the relative strength factor Λ can be estimated from the phase variance at the target according to the formula

$$\Lambda = \frac{\left(1 - e^{-\sigma_\phi^2}\right)}{e^{-\sigma_\phi^2}} = e^{\sigma_\phi^2} - 1,$$

(53)

which is also consistent with the MIF of Reference 2.

Recognizing that the generalized degree of coherence function of Equation (52) consists of the sum of a coherent and incoherent component, the calculated heterodyne efficiency factor given by Equation (18) can likewise be split into the sum of two components. The maximum heterodyne efficiency can be expressed as

$$\varepsilon = \varepsilon_{coh}(1 + \Lambda\sigma_{tar}/\pi a_1 a_2)^{-1} + \varepsilon_{incoh}(1 + \pi a_1 a_2/\Lambda\sigma_{tar})^{-1}, \qquad (54)$$

where σ_{tar} is the total target incoherent LRCS, i.e.,

$$\sigma_{tar} = \iint\limits_{-\infty}^{\infty} d^2\vec{p}\; \frac{d^2\sigma(\vec{p})}{d\vec{p}^2}, \qquad (55)$$

and the coherent and incoherent efficiencies are determined from the relation

$$\varepsilon_{coh/incoh} = \frac{2\beta_r}{(\pi P)^2} \frac{Q_{coh/incoh}}{} \left(1 - e^{-R_m^2(\beta+\beta*)}\right)^{-1} \qquad (56)$$

with the integral factors, $Q_{coh/incoh}$, defined by

$$Q_{coh} = \iiiint\limits_{-\infty}^{\infty} d^2\xi^+ d^2\xi^-\; \theta(R_m^2 - \xi^{+2})\, \theta(R_m^2 - \xi^{-2}) \qquad (57)$$

$$\times \exp[-\beta_r(2\xi^{+2} + \tfrac{1}{2}\xi^{-2}) - \xi^{-2}/\rho_0^2 - i(2\beta_i + kR^{-1})\,\xi^+\cdot\xi^-],$$

and

$$Q_{incoh} = \iiint_{-\infty}^{\infty} d^2\vec{\xi}^+ d^2\vec{\xi}^- \iint_{-\infty}^{\infty} d^2\vec{p} \; \theta(R_m^2 - \xi^{+2}) \; \theta(R_m^2 - \xi^{-2}) \; \frac{d^2\sigma(\vec{p})}{d\vec{p}^2}$$

(58)

$$\times \exp[- \beta_r(2\vec{\xi}^{+2} + \tfrac{1}{2} \vec{\xi}^{-2}) - \vec{\xi}^{-2}/\rho_o^2 - i(2\beta_i + kR^{-1}) \; \vec{\xi}^+ \cdot \vec{\xi}^- - ikR^{-1}\vec{p} \cdot \vec{\xi}^-],$$

where the subscripts r and i on the parameter β denote the real and imaginary parts, respectively. Because the coherent component of the degree-of-coherence function is in the form of a Schell-model MIF, the results of Section 5.2 can be used to express the coherent integral factor in the more condensed form

$$Q_{coh} = 4\pi^2 \int_o^{R_m} \int_o^{R_m} \xi d\xi \, \xi' d\xi' \; I_o\left(\frac{2\xi\xi'}{\rho_o^2}\right) e^{-\alpha_1 \xi'^2 - \alpha_1^* \xi'^2} ,$$

(59)

where

$$\alpha_1 = i\left\{ \frac{k}{2R} + \frac{4z'L'^{-4}}{[1 + (4z'L'^{-2}]} \right\} + \rho_o^{-2}.$$

(60)

To numerically evaluate the incoherent component of the heterodyne efficiency, it is necessary to simplify the incoherent integral factor, Equation (58). Noting the Fourier kernel in the integral of Equation (58), the convolution theorem can be employed to write

21

$$Q_{incoh} = \iint_{-\infty}^{\infty} d^2\vec{\xi}^+ \; e^{-2\beta_r \vec{\xi}^{+2}} \; \theta(R_m^2 - \xi^{+2}) \; \frac{1}{(2\pi)^2} \iint_{-\infty}^{\infty} d^2\vec{\mu}' \; \widetilde{F}(\vec{\mu} - \vec{\mu}') \; \widetilde{E}(\vec{\mu}') \;,$$

<div align="right">(61)</div>

where

$$\vec{\mu} = (2\beta_i + kR^{-1})\vec{\xi}^+ \;,$$

<div align="right">(62)</div>

$$\widetilde{F}(\vec{\mu}') = \iint_{-\infty}^{\infty} d^2\vec{\xi}^- \; d^{-1}\vec{\mu}' \cdot \vec{\xi}^- \; \theta(R_m^2 - \xi^{-2}) e^{-(\frac{1}{2}\beta_r + \rho_o^{-2})(\vec{\xi}^{-2})} \;,$$

<div align="right">(63)</div>

and

$$\widetilde{E}(\vec{\mu}') = \iint_{-\infty}^{\infty} d^2\vec{\xi}^- \; e^{-i\vec{\mu}' \cdot \vec{\xi}^-} \iint_{-\infty}^{\infty} d^2\vec{p}^+ \; e^{-\frac{ik}{R}\vec{p}' \vec{\xi}^-} \; \frac{d^2\sigma(\vec{p})}{d\vec{p}^2}$$

<div align="right">(64)</div>

$$= (2\pi)^2 \left(\frac{R}{k}\right)^2 \; \frac{d^2\sigma(-Rk^{-1}\vec{\mu}')}{d(Rk^{-1}\vec{\mu}')^2} \;,$$

where the double Fourier transform properties of a function have been utilized to write Equation (64). Employing a change of variables

$$\vec{\zeta}' = Rk^{-1}\vec{\mu}'$$

<div align="right">(65)</div>

so that

$$\vec{\zeta} = \vec{\xi}^{+} (1 + 2 \, Rk^{-1} \, \beta_i) , \qquad (66)$$

Equation (61) is written in the form

$$Q_{incoh} = \iint_{-\infty}^{\infty} d^2\xi^{+} \, e^{-2\beta_r \xi^{+2}} \, \theta(R_m^2 - \xi^{+2}) \iint_{-\infty}^{\infty} d^2\zeta' \, \tilde{F}[kR^{-1} \, (\vec{\zeta}' - \vec{\zeta})] \, \frac{d^2\sigma(-\vec{\zeta}')}{d\vec{\zeta}^2} , \qquad (67)$$

where the function $\tilde{F}$ filters the spatial frequencies of the power spectral density of field fluctuations[4] represented by the scattering distribution $d^2\sigma(\vec{x})/d\vec{x}^2$. The filter function $\tilde{F}$ describes the limited bandpass of spatial frequencies passed by the atmosphere, receiving and local oscillator apertures, and the local oscillator amplitude distribution. Although the convolution theorem can be applied to the integral of Equation (63) to write the filter function in one-dimensional form (after an integration over an angle variable) as

$$\tilde{F}(\vec{\mu}') = \frac{2\pi \, R_m}{\tilde{\beta}} \, e^{-\mu'^2/2\tilde{\beta}} \int_{-\infty}^{\infty} d\mu'' \, J_1(\mu'' \, R_m) \, I_0 \, (\mu'\mu''/\tilde{\beta}) \, e^{-\mu''^2/2\tilde{\beta}} , \qquad (68)$$

where

$$\tilde{\beta} = \beta_r + 2\rho_o^{-2} . \qquad (69)$$

it is desireable to obtain an approximate analytical formula. Appendices A
and B provide derivations for the following approximate formulae:

$$\tilde{F}(\vec{\mu}') \cong F_{sp}(\mu') = 2\pi R_m^2 \frac{J_1(\mu' R_m)}{\mu' R} \qquad \text{when } \mu' >> \tilde{\beta} R_m \qquad (.0)$$

$$\tilde{F}(\vec{\mu}') \cong \tilde{F}_E(\mu') \cong 2\pi \left[e^{-\frac{1}{2}\mu'^2/\tilde{\beta}} (\tilde{\beta})^{-1} - e^{-\frac{1}{2}R_m^2(\tilde{\beta}+\frac{1}{2}\mu'^2)} (\tilde{\beta} + \frac{1}{2}\mu'^2)^{-1} \right]$$
$$\text{when } \frac{1}{2}\mu'^2 << \tilde{\beta} \; . \qquad (71)$$

Numerical calculation (illustrated in Section 6) of the filter function and
the approximations given in Equations (70) and (71) show that the following
combination of these approximations provides an excellent estimate of the
exact expression [Equation (68)]:

$$F(\vec{\mu}') = \begin{cases} F_{sp}(\mu') & \mu' > \tilde{\beta} R_m \\ \tilde{F}_E(\mu') & \mu' < \tilde{\beta} R_m \end{cases} \qquad . \qquad (72)$$

It is easy to demonstrate using the approximate forms for the filter function
that

$$\varepsilon_{incoh} \xrightarrow[R_m \to 0]{} 1 \qquad (73)$$

and

$$\varepsilon_{incoh} \xrightarrow[R_m \to \infty]{} 0 \qquad (74)$$

as required from the physics of the problem.

5.4 Target Scattering Properties

5.4.1 Spherical Target Schell-Model Approximation

Because of the approximate analytical results [Equation (45)] obtained for the heterodyne signal resulting from a Schell-model MIF and the relative simplicity of the exact Schell-model efficiency expressions [Equations (47) - (48)], it is desireable to obtain an expression for the Schell-model MIF at the receiver aperture that simulates a target scattering problem of interest. Spheres provide excellent targets for laser radar experiments because the scattering is independent of target orientation. The following development provides expressions for a Schell-model MIF that approximates the MIF arising from scattering from spherical targets.

Reference 2 provides a derivation of the MIF arising from a partially coherent beam-wave source propagating through atmospheric turbulence. The derived field-point MIF is given by

$$
\Gamma^{turb}(\vec{P}^+, \vec{P}^-) = U_o^2 \cos^2\theta F D_1^{-1} \left\{ \exp - (L_A')^{-2}_{inc} \left[2|\vec{P}_y^+|^2 + \frac{1}{2} |\vec{P}_y^-|^2 \right] \right.
$$

$$
- \rho_{inc}'^{2} |P_y^-|^2 - ik (L_\phi')_{inc} \vec{P}_y^+ \cdot \vec{P}_y^- \left. \right\}
$$

$$
+ U_o^2 \cos^2\theta\, e^{-\sigma_\phi^2} D_2^{-1} \exp \left\{ - (L_A')^{-2}_{coh} \left[2|\vec{P}_y^+|^2 + \frac{1}{2} |\vec{P}_y^-|^2 \right] \right.
$$

$$
- \rho_{coh}'^{2} |P_y^-|^2 - ik(L_\phi')_{coh} \vec{P}_y^+ \cdot \vec{P}_y^- \left. \right\}, \tag{75}
$$

where $\vec{P}_y^+$ and $\vec{P}_y^-$ are the y components of the sum and difference field-point coordinates, i.e.,

$$
\vec{P}^+ = \frac{1}{2} (\vec{P}_1 + \vec{P}_2) \tag{76}
$$

and

$$\vec{P}^- = \vec{P}_1 - \vec{P}_2, \tag{77}$$

so that

$$P_y^+ = - R \sin\theta \tag{78}$$

and

$$P_y^- = R\delta \cos\theta, \tag{79}$$

where

$$\delta = \theta - \theta'. \tag{80}$$

The MIF is calculated in terms of the y component (i.e., $\vec{P}_{1x} = \vec{P}_{2x} = 0$) because it contains the interesting angular (θ) dependence. The effective amplitude (L_A') and curvature radii (L_ϕ) as well as the coherence lengths (ρ') in Equation (75) are given by:

$$(L_A')_{inc} = L_A \left[z^2 \left(\rho_o^{-2} \cos^2\theta + \rho_u^{-2} \right) + |1 + i\alpha R|^2 \right]^{1/2}, \tag{81}$$

$$(L_A')_{coh} = L_A \left[z^2 \rho_o^{-2} + |1 + i\alpha R|^2 \right]^{1/2}, \tag{82}$$

$$(L_\phi')_{inc} = R \left[Z^2 \left(\rho_o^{-2} \cos^2\theta + \rho_u^{-2} \right) + |1 + i\alpha R|^2 \right] \left[\text{Im } \alpha R - |\alpha|^2 R^2 - Z^2 \right.$$

$$\left. \times \left(\rho_o^{-2} \cos^2\theta + \rho_u^{-2} - \frac{1}{2} \rho_o^{-2} \right) \right]^{-1}, \qquad (83)$$

$$(L_\gamma')_{coh} = R \left[Z^2 \rho_o^{-2} \cos^2\theta + |1 + i\alpha R|^2 \right] \left[\text{Im } \alpha R - |\alpha|^2 R^2 - Z^2 \rho_o^{-2} \cdot \left(\cos^2\theta - \frac{1}{2} \right) \right]^{-1} \qquad (84)$$

$$\rho_{inc}' = Z \left[Z^2 \left(\rho_o^{-2} \cos^2\theta + \rho_u^{-2} \right) + |1 + i\alpha R|^2 \right]^{1/2} \left[\rho_o^{-2} Z^2 \sec^2\theta \left(1 - 2 R \text{ Im}\alpha + |\alpha|^2 R^2 \right) \right.$$

$$\qquad (85)$$

$$\left. + \rho_o^{-2} Z^2 \left(R \text{ Im}\alpha + \frac{3}{4} Z^2 \rho_o^{-2} - \sin^2\theta \right) + \rho_u^{-2} Z^2 \left(1 + \rho_o^{-2} Z^2 \sec^2\theta \right) \right]^{-1/2},$$

and

$$\rho_{coh}' = Z \left[Z^2 \rho_o^{-2} \cos^2\theta + |1 + i\alpha R|^2 \right]^{1/2} \left[\rho_o^{-2} Z^2 \sec^2\theta \left(1 - 2 R \text{ Im}\alpha + |\alpha|^2 R^2 \right) \right.$$

$$\qquad (86)$$

$$\left. + \rho_o^{-2} Z^2 \left(R \text{ Im}\alpha + \frac{3}{4} Z^2 \rho_o^{-2} - \sin^2\theta \right) \right]^{-1/2},$$

where

$$Z^2 = 2 \left(\frac{2R}{kL_A} \right)^2 , \qquad (87)$$

$$F = 1 - e^{-\sigma_\phi^2}, \tag{88}$$

$$D_1 = \left\{ \left[z^2 \left(\rho_o^{-2} + \rho_u^{-2} \right) + |1 + i\alpha R|^2 \right] \left[z^2 \left(\rho_u^{-2} + \rho_o^{-2} \cos^2\theta \right) + |1 + i\alpha R|^2 \right] \right\}^{1/2}$$

and

$$D_2 = \left\{ \left[\rho_o^{-2} z^2 + |1 + i\alpha R|^2 \right] \left[z^2 \rho_o^{-2} \cos^2\theta + |1 + i\alpha R|^2 \right] \right\}^{1/2}. \tag{90}$$

Approximate values of the source amplitude radius (L_A) and phase curvature radius (L_ϕ) are derived below such that the assumed Schell-model source emulates the known scattering properties of a sphere.

The scattering cross section of a target is defined by the relation

$$\sigma_{tar}(\vec{P}) = \lim_{R \to \infty} 4\pi R^2 \frac{\left\langle U_s(\vec{P}) \, U_s^*(\vec{P}) \right\rangle}{|U_i|^2}. \tag{91}$$

The scattering cross section of a perfectly specular sphere is given by

$$\sigma_{tar}(\vec{P}) \Big|_{\substack{specular \\ sphere}} = \pi L_{sp}^2 \tag{92}$$

(where L_{sp} is the sphere radius) when the sphere is large with respect to a wavelength. Thus, a necessary requirement for the Schell-model source sphere simulation is

$$\pi L_{sp}^2 = \lim_{R \to \infty} 4\pi R^2 D_2^{-1}$$

$$= \frac{4\pi}{|\alpha|^2} = 4\pi \left[\frac{4}{k^2 L_A^2} + \frac{1}{L_{sp}^2} \right]^{-1}. \tag{93}$$

The sphere radius has been used for the phase front curvature in Equation (93) because of the known curvature of a wave front scattered by a sphere. The Equation (93) requirement yields

$$L_A \Big|_{\substack{\text{specular} \\ \text{sphere}}} = L_{Asp} = \left(\frac{2 L_{sp}}{k} \right)^{1/2} 3^{-1/4} = 1.07 \sqrt{\frac{L_{sp}}{k}}. \tag{94}$$

The predicted amplitude radius of Equation (94) is approximately equal to the first Fresnel zone of the sphere which is consistent with the physical optics prediction of specular scattering from a sphere.

The cross section associated with the incoherent (i.e., diffuse) component of scattering from a sphere can be estimated by integrating the diffuse differential cross section over the observed sphere surface area. Because the cross section per unit illuminated area (σ^0) is related to the bidirectional reflectance distribution function (ρ'_{BRDF}) by the relation[7]

$$\sigma^0 = 4\pi \rho'_{BRDF} \cos\theta \cos\theta', \tag{95}$$

the diffuse sphere cross section is

$$\sigma_{tar}(\vec{P})\Bigg|_{\substack{\text{diffuse}\\\text{sphere}}} = \int dA \; \sigma^o \; (\theta = -\theta')$$

$$= 2\pi L_{sp}^2 \int_{0}^{\pi/2} d\theta \sin\theta \; \sigma^o \; (\theta = -\theta') \tag{96}$$

$$= 8\pi^2 L_{sp}^2 \int_{0}^{\pi/2} d\theta \sin\theta \; \cos^2\theta \; \rho'_{BRDF} \; (\theta = -\theta').$$

If a surface scatters all the energy incident upon it in accordance with Lambert's law with half of the scattered power in each of two orthogonal polarization components, the bidirectional reflectance distribution function is a constant equal to $(2\pi)^{-1}$. Thus, the cross section associated with a Lambertian spherical scattering surface is

$$\sigma_{tar}\Bigg|_{\substack{\text{Lambertian}\\\text{sphere}}} = 4\pi L_{sp}^2 \int_{0}^{\pi/2} \sin\theta \cos^2\theta \, d\theta = \frac{4}{3}\,\pi L_{sp}^2 \; . \tag{97}$$

Because the Lambertian sphere cross section is within a factor of 1/3 of the specular sphere cross section, it is reasonable to estimate the cross section for the diffuse scattering cross section by πL_{sp}^2 regardless of the reflectance distribution function of the surface. Thus a Schell-model approximation of the scattering MIF resulting from a spherical target is obtained by using the relations

$$D_1 \sim D_2 \approx 4R^2/L_{sp}^2 \tag{98}$$

in Equation (75) along with the requirements that

$$L_\phi \cong L_{sp} \tag{99a}$$

$$L_A \bigg|_{\substack{\text{coherent} \\ \text{component}}} \cong 1.07 \ \frac{L_{sp}}{k} \tag{99b}$$

$$L_A \bigg|_{\substack{\text{incoherent} \\ \text{component}}} \cong L_{sp} \tag{99c}$$

in Equations (81) – (87). The final relationship [Equation (99c)] arises from the requirement that the amplitude radius for the diffuse scattering process must be the the same order of magnitude as the actual sphere radius.

A check on the validity of the spherical source Schell-model approximation is obtained by calculating the coherence length arising from the incoherent component without atmospheric turbulence (i.e., $C_n^2 = 0$). It is straightforward to show that for a range much larger than a sphere radius and a target coherence length less than a wavelength,

$$\rho'_{inc} \bigg|_{\substack{\text{Schell} \\ \text{model}}} \cong z \bigg|_{\text{incoherent}} \cong \frac{\sqrt{2} \ 2R}{kL_{sp}} = \frac{2.8R}{kL_{sp}} \tag{100}$$

when

$$(k\rho_u) < 1. \tag{101}$$

This result can be compared with the coherence length arising from a uniformly illuminated disc (corresponding to the brightness distribution of a Lambertian sphere). The degree-of-coherence function for a uniform disc source is

$$\gamma(\delta) \sim \frac{2 \, J_1\left(kL_{sp}\delta\right)}{kL_{sp}\delta} .$$ (102)

The e^{-1} value of the Equation (102) distribution occurs for an argument of the Bessel function of approximately 2.5. Thus the Lambertian sphere coherence length of

$$\rho'_{inc}\bigg|_{\substack{\text{Lambertian} \\ \text{sphere}}} \cong \frac{2.5R}{kL_{sp}}$$ (103)

is in good agreement with the Schell-model approximation result. It is also straightforward to show that the predicted coherence length of the coherent component correctly models coherent spherical wave propagation through the atmosphere.

5.4.2 Projected LRCS Distributions for Spheres and Cones

The calculation of the heterodyne efficiency resulting from incoherent target scattering [Equation (67)] requires the functional description of the projected LRCS distribution. If the laser bidirectional reflectance distribution function (or equivalently the cross section per unit area) of the target material is specified, the LRCS distribution can be determined from the target's geometry. The development below illustrates the calculation of LRCS distributions for two simple target geometries: spheres and cones. Subsequent numerical calculations (presented in Section 6) utilize these expressions together with the ROSSCO laser scattering algorithm[7] to specify LRCS distributions for illustrative numerical calculations.

Spheres: The projected differential area, dA_p, resulting from a surface differential area, dA, that is tilted an angle θ from normal with respect to the projection direction is
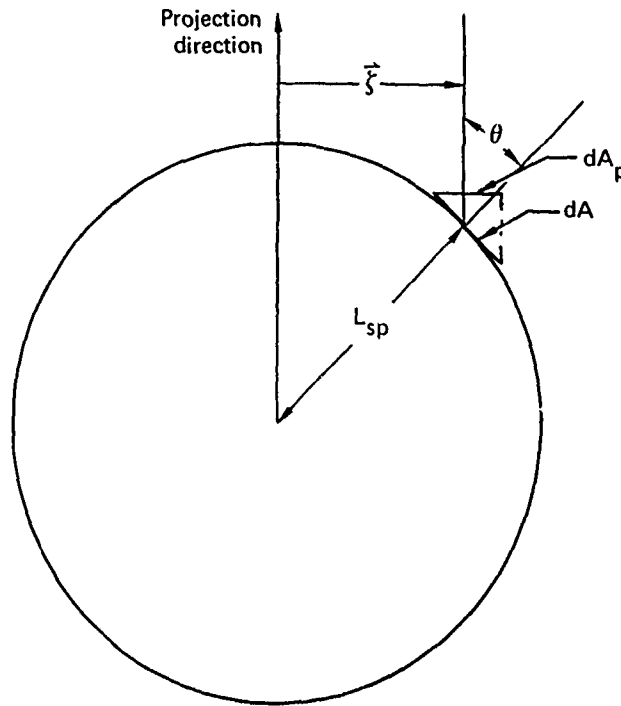
$$dA_p = \cos\theta \, dA. \tag{104}$$

Because a differential surface element of a sphere that is a distance $|\vec{\zeta}|$ radially outward from the projection normal (see Figure 2) is tilted at an angle $\sin^{-1}(|\vec{\zeta}|/L_{sp})$, the distributed LRCS is defined by the relation

$$\left.\frac{d^2\sigma(\vec{\zeta})}{d\vec{\zeta}^2}\right|_{sphere} = \frac{\sigma^o[\theta \cdot \sin^{-1}(|\vec{\zeta}|/L_{sp})]}{\cos\theta} \quad \text{for } |\zeta| < L_{sp}$$

$$\tag{105}$$

$$= 0 \quad \text{for } |\vec{\zeta}| > L_{sp},$$

where the argument of the cross section per unit illuminated area, σ^o, in Equation (105) is the backscatter angle.
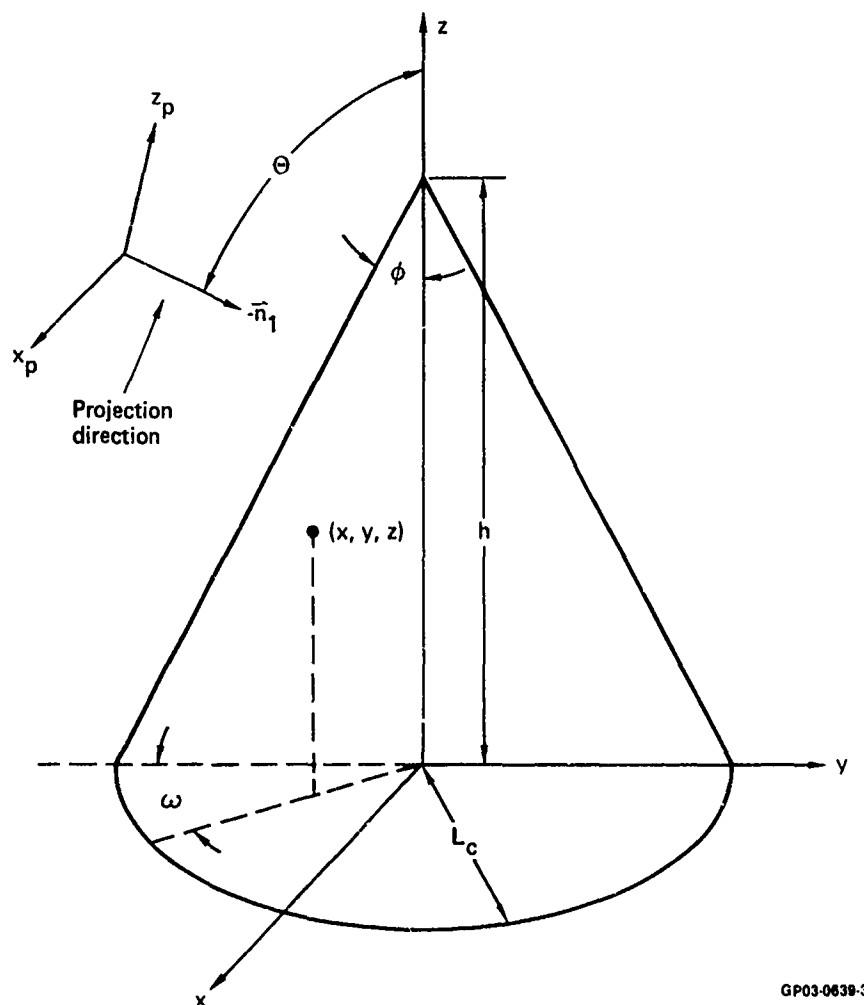
Figure 2. Sphere projection geometry.

Cones: To determine the LRCS distribution of a conical surface, the projection geometry depicted in Figure 3 is employed where x_p and z_p denote the orthogonal coordinates of the projection plane. The surface of the cone is defined by the equation

$$z = \frac{h}{L_c} \left(L_c - \sqrt{x^2 + y^2} \right),$$

(106)

while the polar angle, ω, of a point on the surface of the cone is given by

$$\omega = \tan^{-1} \left(- x/y \right).$$

(107)

Figure 3. Cone projection geometry.

Because the projection coordinate z_p is related to the cone surface coordinates by the transformation relation

$$z_p = z \sin\theta + y \cos\theta, \tag{108}$$

where θ is the projection direction, the equation

$$z_p = \frac{h}{L_c} \left(L_c - \sqrt{x_p^2 + y^2} \right) + y \cos\theta \tag{109}$$

35

relates the projection plane coordinates to the y body coordinate on the surface of the cone. Equation (109) has two solutions for a given projection plane coordinate (x_p, z_p) corresponding to the two intersection points, on the near and far side, of the infinite cone. The scalar product of the projection direction vector, $\vec{n}_1$, with the cone surface normal direction vector yields the following equation for the local surface tilt angle, θ_ℓ:

$$\cos\theta_\ell = \sin\theta \, \cos\omega \, \cos\phi + \cos\theta \, \sin\phi, \tag{110}$$

where

$$\cot\phi = \frac{h}{L_c} . \tag{111}$$

Thus, the projected LRCS distribution is given by

$$\frac{d^2\sigma\left(x_p, \, z_p\right)}{dx_p \, dz_p} = \frac{\sigma^0\left[\theta_\ell\left(x_p, \, z_p\right)\right]}{\cos\left[\theta_\ell\left(x_p, \, z_p\right)\right]} \quad \text{for } \left(x_p, \, z_p\right) = \left(x_p^*, \, z_p^*\right)$$

$$\tag{112}$$

$$= 0 \quad \text{for } \left(x_p, \, z_p\right) \neq \left(x_p^*, \, z_p^*\right),$$

where the $\left(x_p^*, \, z_p^*\right)$ coordinates fall within the projected rectangular outline of the cone defined by the equations

$$- L < x_p^* < L_c$$

$$- L_c \cos\theta < z_p^* < \begin{cases} h \, \sin\theta & \text{if } \theta > \phi \\ L_c \, \cos\theta & \text{if } \theta < \phi, \end{cases} \tag{113}$$

the projection point lies on the surface of the truncated cone defined by

$$y^2(x_p^*, z_p^*) + x_p^{*2} < L_c^2,$$ (114)

and the $y(x_p^*, z_p^*)$ solution of Equation (109) used to solve Equations (107) and (110) is the minimum of the two roots.

6. NUMERICAL RESULTS

To establish some of the functional relations of the expressions derived in Section 5, the results of several numerical computations are presented below in graphical and tabular form. These results illustrate the effects of various transceiver and target scattering parameters on predicted heterodyne performance. The various parameters chosen for these illustrative calculations were selected to provide representative results rather than to model a specific transceiver configuration or target scattering scenario. A wavelength of 10.6 µm was assumed for all computations. Because calculated results were computed with 18 different computer codes that were developed for specific computations in the course of an evolving analytical research program, the codes are not listed in this report.

6.1 Heterodyne Signal Calculations

Figures 4-8 illustrate, in three-dimensional graphical form, the variation in the relative heterodyne signal predicted by the stationary-phase approximation result, Equation (45), (Figures 4a-8a), and the exact two-dimensional integral result, Equation (46) (Figures 4b-8b). Although Figures 4 and 5 demonstrate surprisingly close agreement between the stationary-phase result and the exact result as a function of the local oscillator parameters A and L_0 and the coherence length, r_c, only general features are replicated in the two calculations in Figures 6 and 8 (for the variables f_ℓ, L_ϕ, and r_c), and a totally different functional relation between the focal lengths f_ℓ and f_r is shown in Figure 7. Thus, although the stationary-phase result [Equation (45)] provides an order-of-magnitude estimate for the signal power in an analytic form which can be quickly calculated on a hand calculator, it cannot be used to provide accurate predictions or uniformly valid functional relations.

The general functional trends depicted in the exact-result signal power calculation of Figures 4b-8b can be interpreted from the known physics of the detection process. Figures 4-6 show that an increased coherence length, r_c, of the detected signal always results in an increased signal power since the signal becomes more coherent (the speckle cell dimensionality increases) and hence the phase front becomes more uniform and amenable to the heterodyne detection process. Figures 4 and 5 also demonstrate the increase in signal power as the local-oscillator amplitude radius or aperture radius increases,

38

reflecting the increase in the photodetector area used for the detection
process. The oscillatory behavior shown in Figure 5 as a function of the
local oscillator radius (for a coherent wave) replicates the "ringing"
interference behavior predicted by earlier investigations.[9,10] Figures 6b-8b
shown an increase in the predicted heterodyne signal with decreasing local-
oscillator focal length because the receiving aperture spot-size is larger
than the local-oscillator spot-size on the photodetector (for the assumed
local-oscillator radius), resulting in incomplete heterodyne detection of the
signal enclosed by the receiving aperture. Equivalently, the analysis of
Section 5.2 shows that the back-propagated wave underfills the receiving
aperture when the local-oscillator radius is smaller than required for
complete heterodyne detection of the received signal. It is noteworthy that
Figure 8 shows that the heterodyne signal is relatively unaffected by the
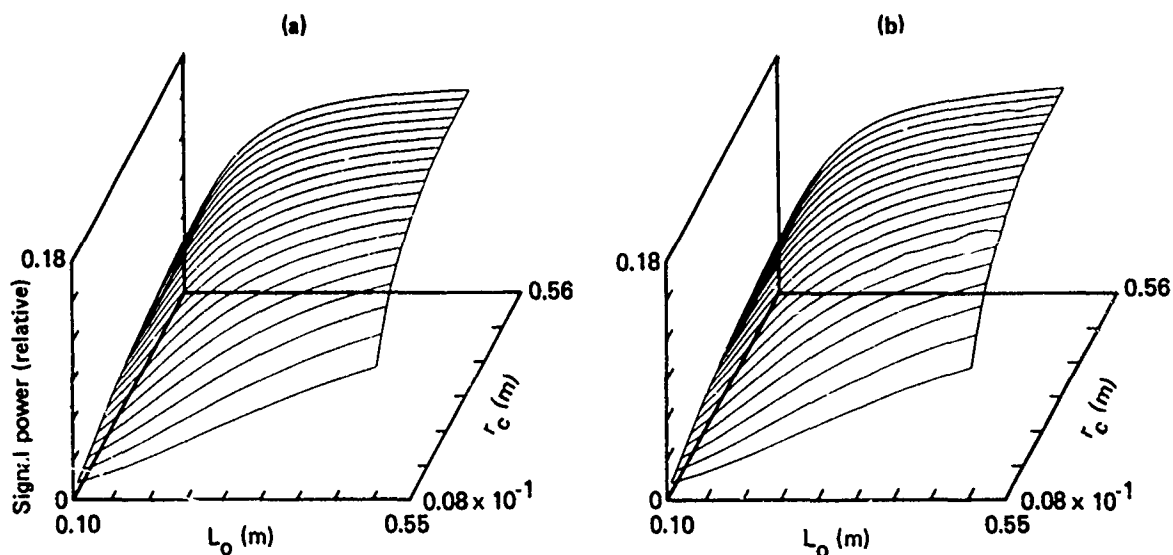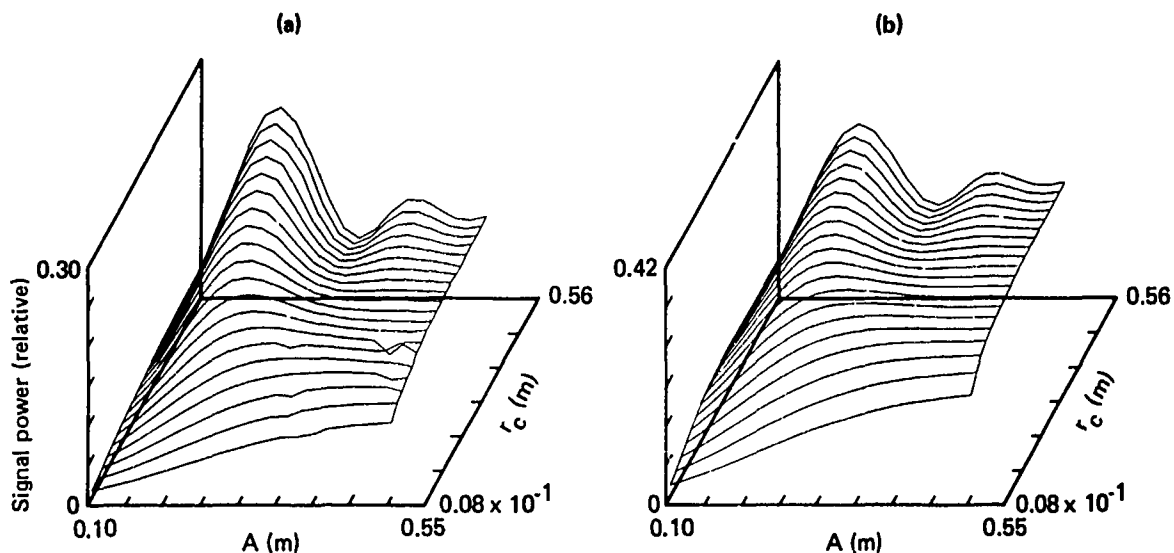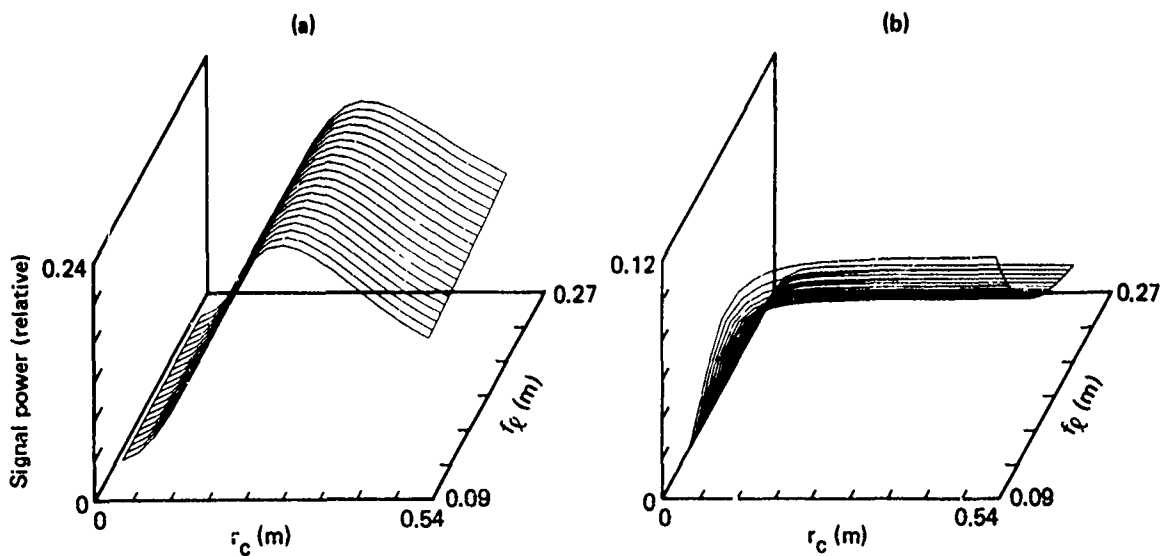phase-front curvature of the received signal.

**Figure 4. Laser heterodyne signal power results calculated by the stationary phase
method (a) and numerical integration technique (b) as a function of the local
oscillator amplitude radius, L_o, and Schell-model coherence length, r_c. Fixed
parameters of the calculation are A = 10 cm, P = 9.5 cm, f_Q = 12.5 cm,
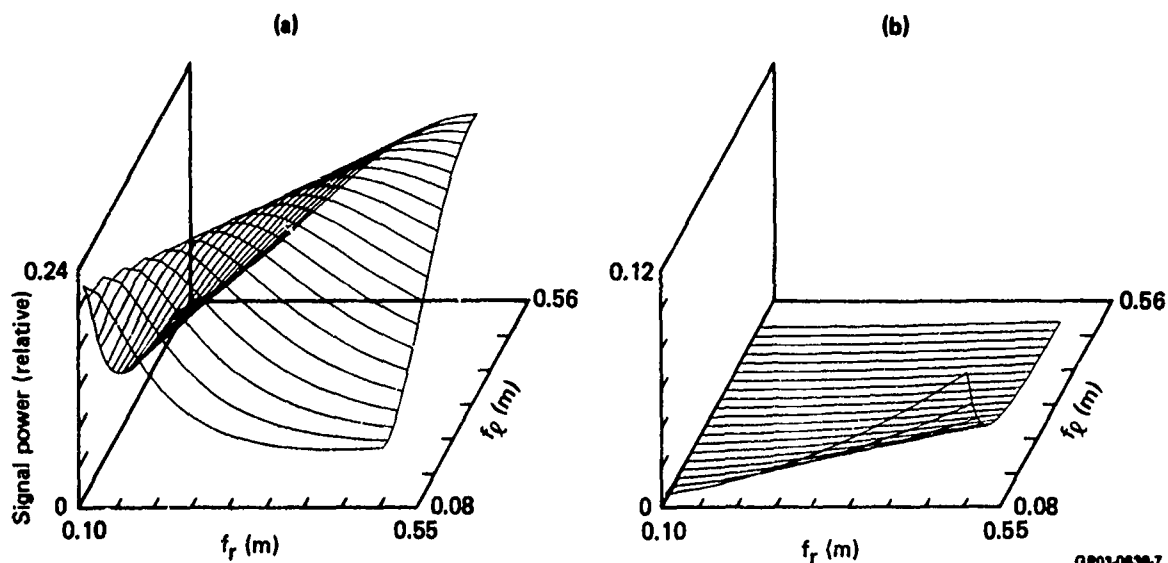f_r = 25 cm, L_ϕ = −200 m, and R = 200 m.**

Figure 5. Laser heterodyne signal power results calculated by the stationary phase
method (a) and numerical integration technique (b) as a function of the
local oscillator aperture radius, A, and Schell-model coherence length, r_c.
Fixed parameters of the calculation are l_o = 8 cm, P = 10 cm, f_ϱ = 12.5 cm,
f_r = 25 cm, L_ϕ = −200 m, and R = 200 m.

Figure 6. Laser heterodyne signal power results calculated by the stationary phase (a)
and numerical integration technique (b) as a function of the local
oscillator focal length, f_ϱ, and Schell-model coherence length, r_c. Fixed
parameters of the calculation are A = 2 mm, P = 2.5 cm, L_o = 8 cm,
f_r = 25 cm, L_ϕ = −200 m, and R = 200 m.

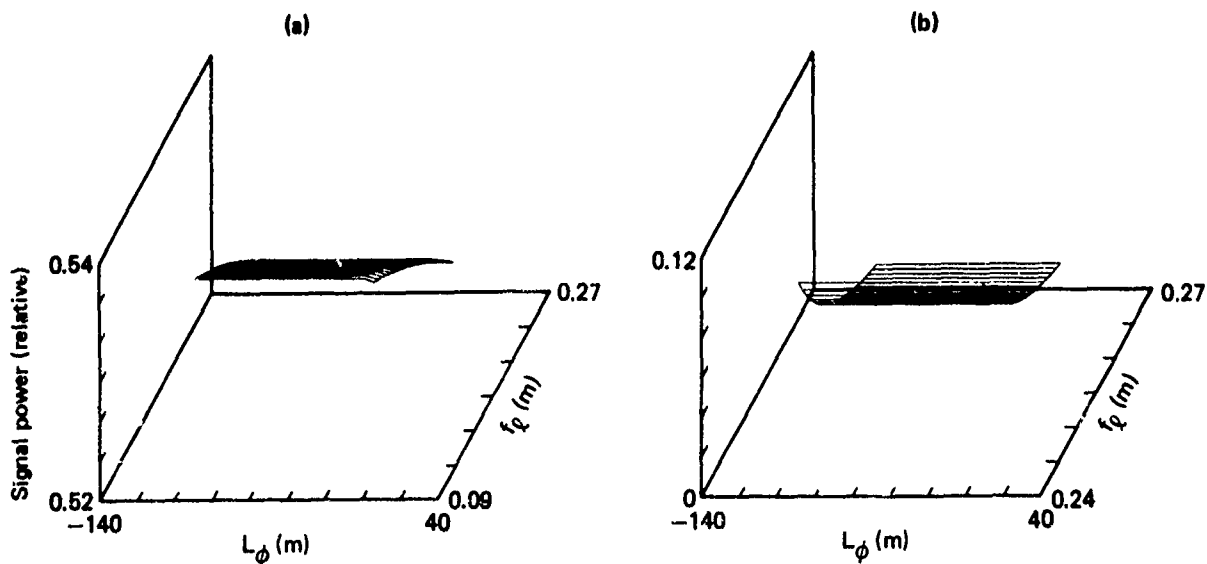**Figure 7.** Laser heterodyne signal power results calculated by the stationary phase (a) and numerical integration technique (b) as a function of the local oscillator focal length, f_ϱ, and receiver focal length, f_r. Fixed parameters of the calculation are A = 2 mm, P = 2.5 cm, L_o = 2.5 cm, r_c = 0.5 m, L_ϕ = –200 m, and R = 200 m.


Figure 8. Laser heterodyne signal power results calculated by the stationary phase (a) and numerical integration technique (b) as a function of the local oscillator focal length, f_ϱ, and phase front curvature, L_ϕ. Fixed parameters of the calculation are A = 2 mm, P = 2.5 cm, L_o = 2.5 cm, f_r = 25 cm, r_c = 1 cm, and R = 200 mm.

41

6.2 Heterodyne Efficiency for Schell-Model Sources

Figures 9-11 show representative results for the calculated maximum heterodyne efficiency, Equation (48), as a function of the local-oscillator parameters, A and L_0, the coherence length, r_c, and the focal length f_ℓ and f_r. Similar results are depicted in Figures 9 and 10: heterodyne efficiency decreases with decreasing effective local-oscillator aperture and coherence length. Figures 9 and 10 show that increasing the local-oscillator amplitude radius, L_0, (for sufficiently large aperture) or increasing the local-oscillator aperture, A, (for sufficiently large amplitude radius) will result in an increased detection efficiency until a condition is obtained where the back-propagated local-oscillator beam overfills the receiving aperture, after which no efficiency benefits are obtained. The primary difference between Figures 9 and 10 is the more gradual increase in the heterodyne efficiency with increasing local-oscillator amplitude radius vis-a-vis aperture size. The Figure 11 plot of the heterodyne efficiency as a function of the local-oscillator and receiver focal length again illustrates the requirement that the back-propagated local-oscillator beam must overfill the receiving aperture for optimum signal-to-noise ratio efficiency. Thus optimum heterodyne efficiency is generally obtained when the local-oscillator amplitude radius is large and the local-oscillator aperture truncates the Gaussian beam profile such that the image of the aperture at the receiving lens is larger than the entrance pupil.

Figure 12 provides a graph of the computed maximum heterodyne efficiency, Equation (48), as a function of the sphere radius and source coherence length used in the Schell-model approximation of the radiation characteristics arising from laser scattering by spheres (Section 5.4.1). Whereas previous Figures (4, 5, 6, 9, 10) show the decrease in heterodyne efficiency with decreasing coherence length, Figure 12 depicts the coherence length effects on the efficiency resulting from target parameters. The source coherence length, ρ_u, used in Schell-model sphere approximation parameterizes the coherence length arising from the laser scattering process and thus relates to the surface-height correlation length for a rough-surface scattering process. Clearly, large source coherence lengths (much larger than a wavelength) describe scattering from smooth surfaces, whereas small source coherence lengths result from diffuse (rough surface) scattering processes.

42

The results plotted in Figure 12 demonstrate that maximum heterodyne efficiency is achieved for sphere scattering when either the sphere radius is small or the surface is very smooth. It is also noteworthy that Figure 12 indicates that large spheres must be smoother than smaller spheres to achieve comparable heterodyne efficiency.
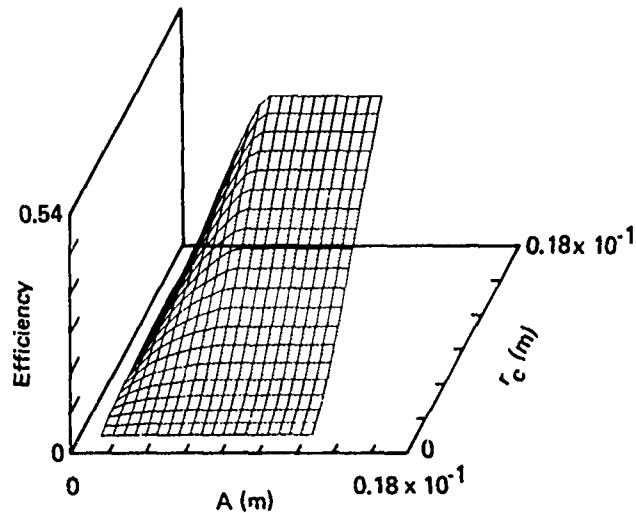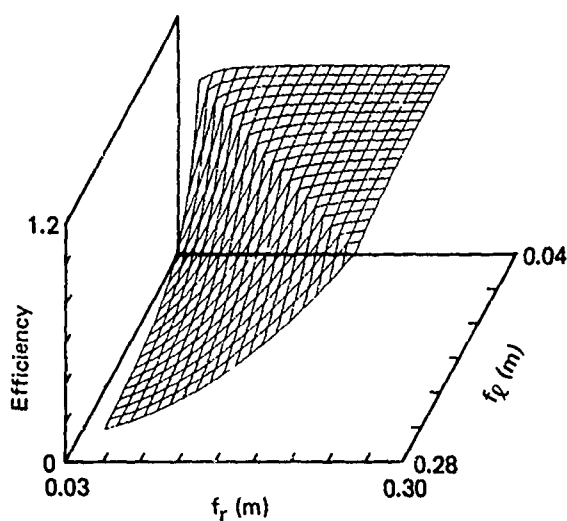

GP03-0639-11

Figure 9. Calculated laser heterodyne maximum detection efficiency as a function of the local oscillator aperture radius, A, and Schell-model coherence length, r_c. Fixed parameters of the calculation are L_o = 1.25 cm, P = 1.25 cm, f_ϱ = 12.5 cm, f_r = 25 cm, L_ϕ = −200 m, and R = 200 m.
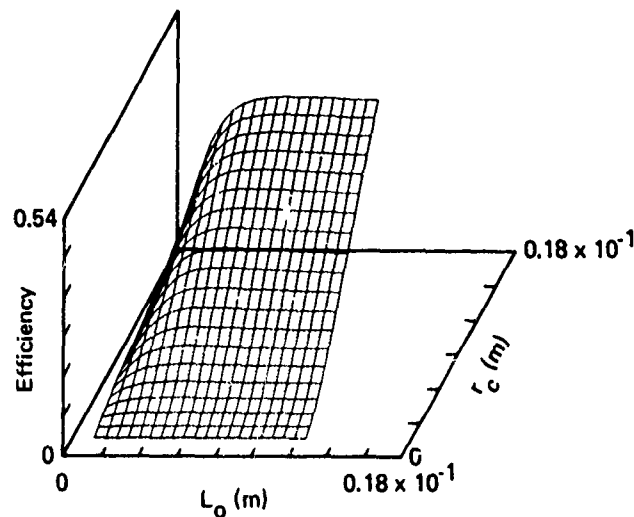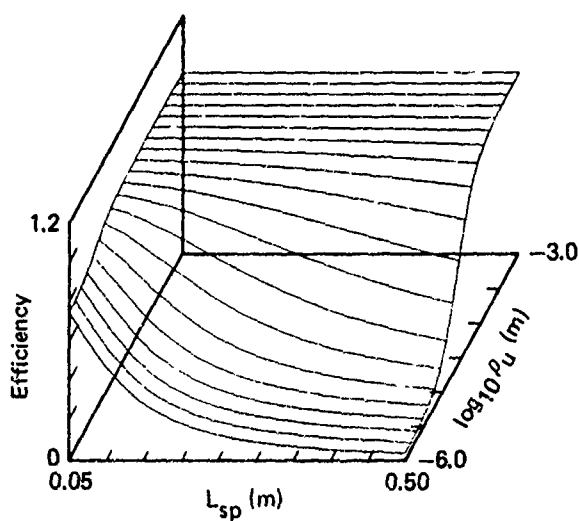

GP03-0639-12

Figure 10. Calculated laser heterodyne maximum detection efficiency as a function of the local oscillator amplitude radius, L_o, and Schell-model coherence length, r_c. Fixed parameters of the calculation are A = 1.25 cm, P = 1.25 cm, f_ϱ = 12.5 cm, f_r = 25 cm, L_ϕ = −200 m, and R = 200 m.

43

GP03-0639-10

Figure 11. Calculated laser heterodyne maximum detection efficiency as a function of
the local oscillator focal length, f_{ϱ}, and receiver focal length, f_r. Fixed
parameters of the calculation are L_0 = 1.25 cm, P = 1.25 cm, A = 1.25 cm,
r_c = 1 m, L_{ϕ} = -200 m, and R = 200 m.

GP03-0639-9

Figure 12. Calculated laser heterodyne maximum detection efficiency as a function of
a spherical targets radius, L_{sp}, and scattered laser coherence length, ρ_u. Fixed
parameters of the calculation are P = 2.5 cm, L_0 = 2.5 cm, A = 2.5 cm,
f_r = 25 cm, f_{ϱ} = 25 cm, R = 500 m, C_n^2 = 10^{-15} $m^{-2/3}$, σ_{ϕ} = 5.0. The
illuminating laser beam is assumed to have a focal length of -25.0 m and a
2.5 cm aperture radius.

44

6.3 Heterodyne Efficiency for General LRCS Distributions
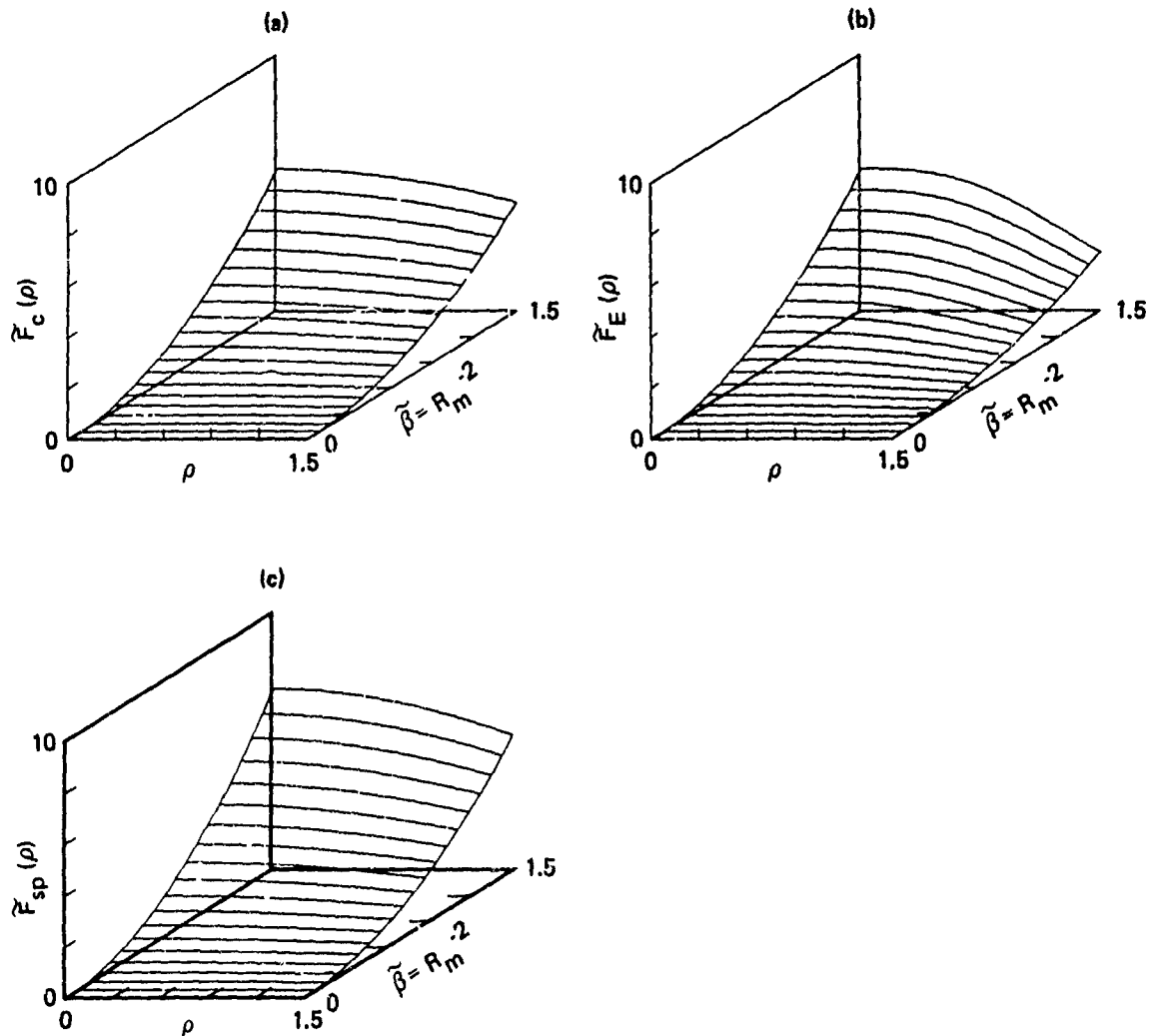
6.3.1 Filter Function Approximation

To account for the effects of atmospheric turbulence and finite local oscillator amplitude radius in the general calculation of the heterodyne efficiency [Equations (56) and (58)], it was necessary to develop an approximate form for the filter function [Equation (72)] to reduce the exact six-fold dimensional integral, Equation (58), to a more numerically tractable four-fold form [Equation (67)]. Figures 13 and 14 provide graphs of (a) the exact filter function [Equation (68)], (b) the stationary-phase approximate result [Equation (70)] (Appendix A), and (c) the series-expansion approximate result [Equation (71)] (Appendix B) as a function of the unitless variable $\rho = R_m \mu'$ and the scaling parameter $\tilde{\beta} = R_m^{-2}$ for a relatively short range of ρ (Figure 13) and a more extended range of ρ (Figure 14). The results plotted in Figures 13 and 14 demonstrate that the series-expansion result replicates the exact result for values of ρ less than unity, whereas the stationary-phase result closely approximates the exact result for ρ values in excess of unity as stated by the Equation (72) approximation.

To illustrate the degree-of-accuracy of the filter-function approximation as it affects heterodyne efficiency calculations, Figure 15 provides a comparison of the heterodyne efficiency calculated by the exact two-fold integral analysis [Equation (48)] with the corresponding efficiency calculated by the four-fold integral [Equations (56) and (67)], assuming a comparable Gaussian source LRCS distribution. The Figure 15 data demonstrate that efficiency results can be computed using the general four-fold integral method which closely approximates results obtained with a more exact (two-fold integral) technique of limited applicability.

### 6.3.2 Atmospheric Turbulence Effects

Figure 16 illustrates the predicted effects of atmospheric turbulence on heterodyne efficiency for (a) a glint return [Equations (56) and (59)] and (b) the return from a small (1 cm radius) spherical target [Equations (56) and (67)] as a function of the range to the target. The Figure 16 data demonstrate that although atmospheric turbulence decreases the heterodyne detection efficiency, especially at long ranges (~ 10 km), the degradation in

signal-to-noise ratio is relatively minor compared with diffuse target speckle effects. The computed results plotted in Figure 16b also demonstrate that the heterodyne efficiency computed for the small sphere (using the approximate four-fold integral method) closely approximates the glint return results, substantiating the validity of the approximate filter function for turbulence effects calculations.

Figure 13. Laser radar filter function calculated by (a) numerical integration, (b) series expansion, and (c) stationary phase approximation as a function of the unitless variable $\rho = R_m \mu'$ and the parameter $\tilde{\beta} = R_m^{-2}$.
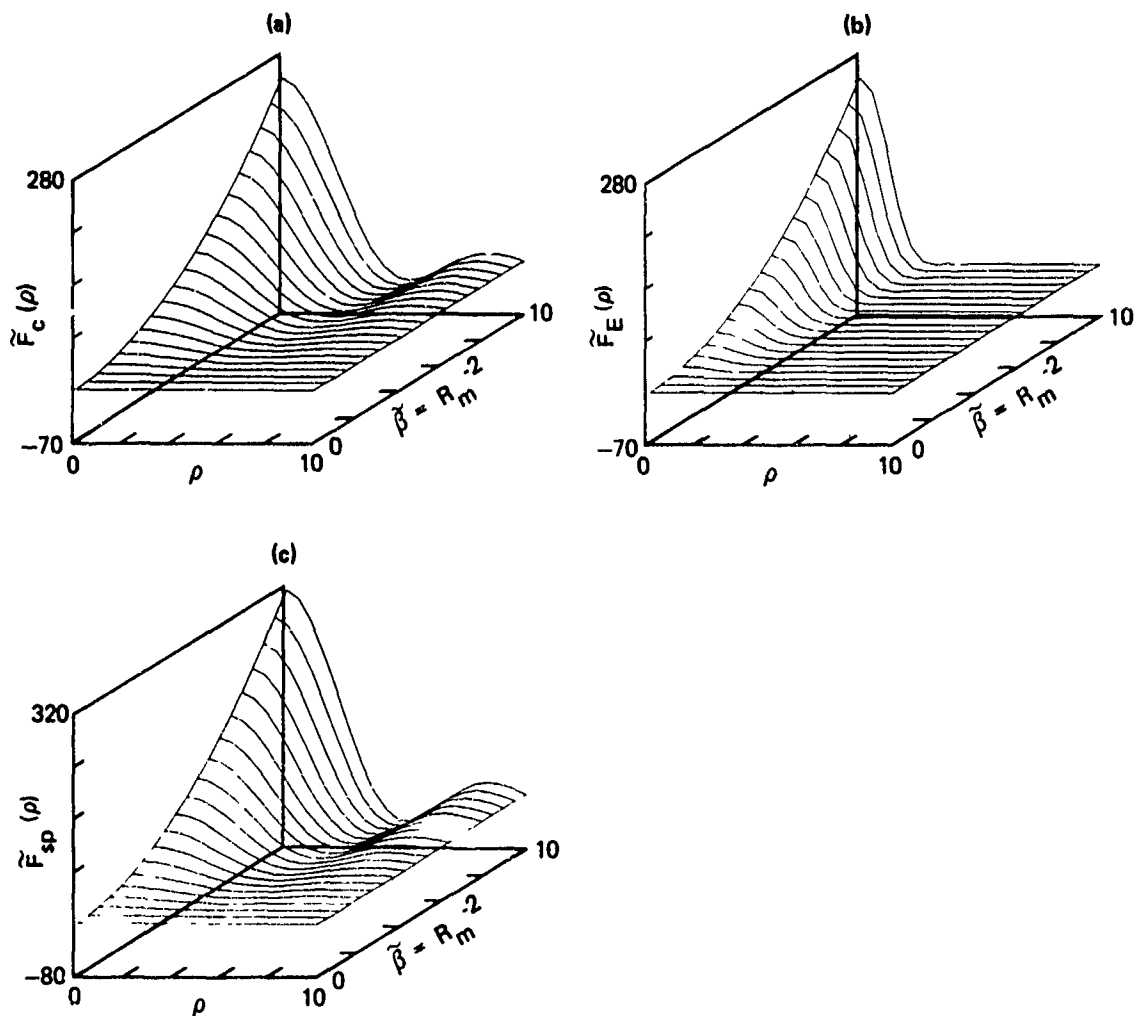
Figure 14. Laser radar filter function calculated by (a) numerical integration, (b) series expansion, and (c) stationary phase approximation as a function of the unitless variable $\rho = Rm\mu'$ and the parameter $\widetilde{\beta} = R_m{}^{-2}$.

GP03-0630-14

47
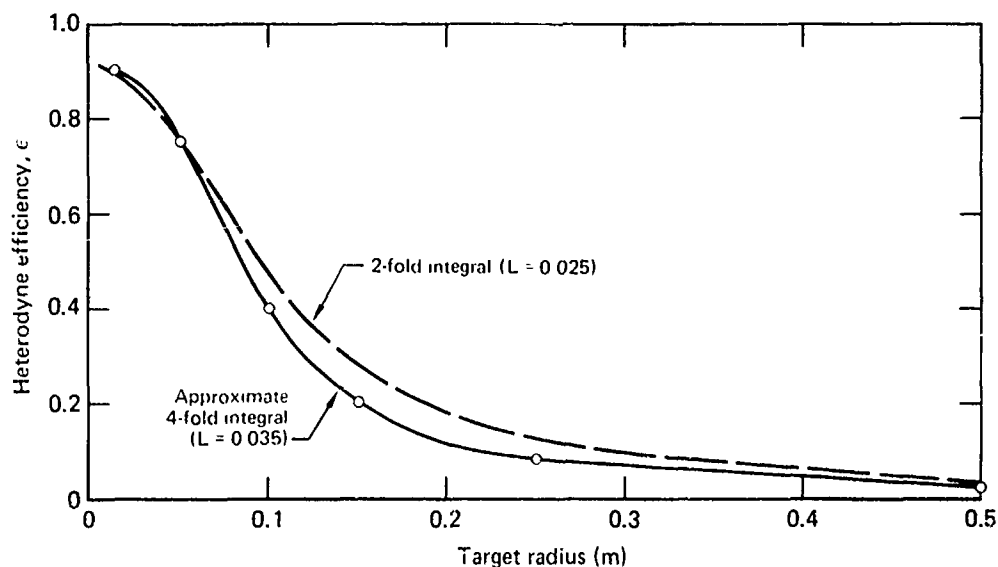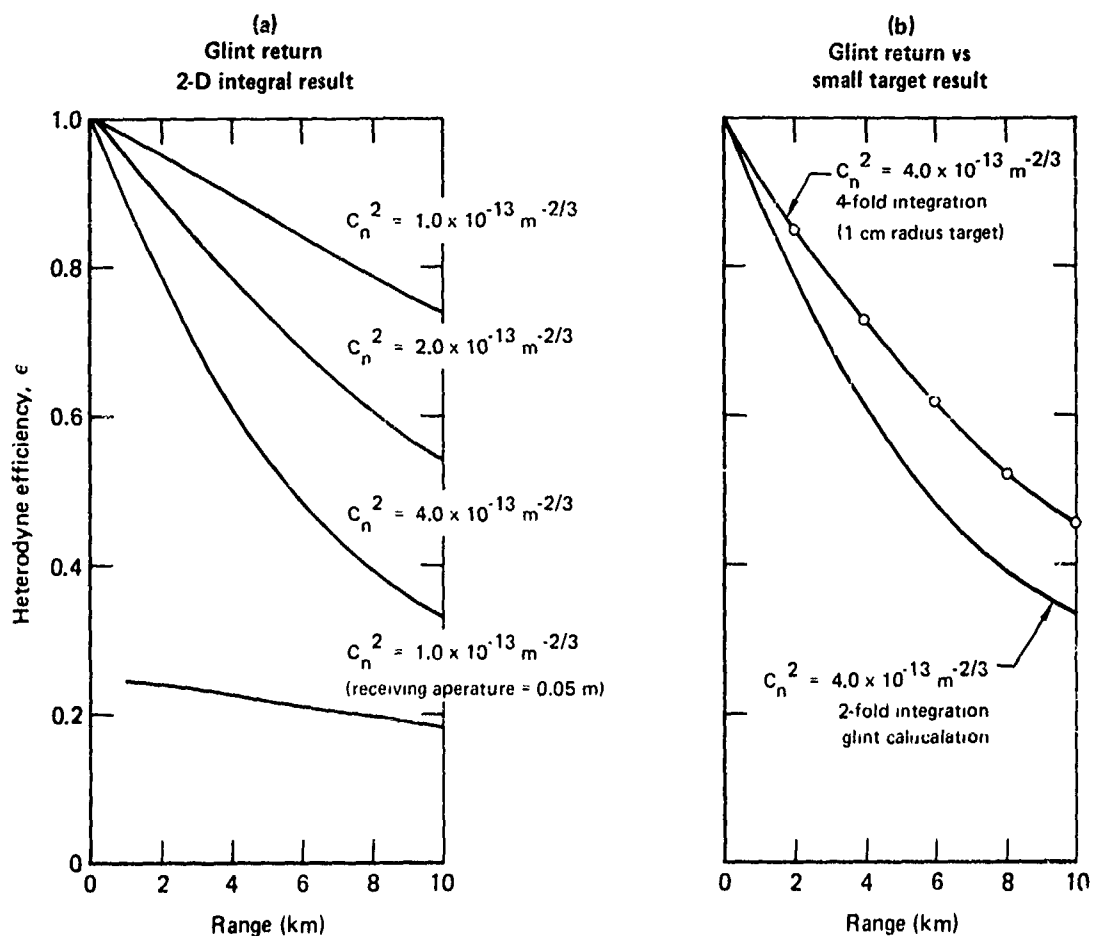
Figure 15. Calculated laser heterodyne maximum detection efficiency as a function of
the radius of a Schell-model source. Fixed parameters of the calculation are
$A = P = 2.5$ cm, $f_{\ell} = f_r = 25$ cm, and $R = 500$ m.

6.3.3 Target Reflectivity Calculations

To provide a data file of representative target LRCS distributions for
subsequent studies of target effects on heterodyne-detection efficiencies, a
set of representative (yet hypothetical) rough-surface reflectivities was
defined using the ROSSCO laser scattering algorithm[7], and various projected
LRCS distributions were calculated using the projection equations developed in
Section 5.4.2. Figure 17 depicts the backscatter bidirectional reflectance
distribution functions that are predicted by the ROSSCO algorithm for metallic
surfaces having a small-scale surface roughness described by an exponential
surface-height power spectral density function (with varying correlation
lengths) and a Gaussian surface-height probability density function. These
functions assumed characteristics of the small-scale roughness correspond to
measured properties of many machined and industrially processed metallic
materials.[11] The hypothetical rough surfaces are numbered 1 through 4 in
increasing order of smoothness. Figure 18 provides three-dimensional graphs
of the spherical-surface LRCS distribution function, Equation (105), for the
same metallic surfaces. The distributions plotted in Figure 18 show the
transition from a nearly uniform circular LRCS distribution for a rough
sphere, Figure 18a, to the point-like distribution for a very smooth sphere,
Figure 18d.

48

(a)
Glint return
2-D integral result

(b)
Glint return vs
small target result

$C_n^2 = 1.0 \times 10^{-13} \text{ m}^{-2/3}$

$C_n^2 = 2.0 \times 10^{-13} \text{ m}^{-2/3}$

$C_n^2 = 4.0 \times 10^{-13} \text{ m}^{-2/3}$

$C_n^2 = 1.0 \times 10^{-13} \text{ m}^{-2/3}$
(receiving aperature = 0.05 m)

$C_n^2 = 4.0 \times 10^{-13} \text{ m}^{-2/3}$
4-fold integration
(1 cm radius target)

$C_n^2 = 4.0 \times 10^{-13} \text{ m}^{-2/3}$
2-fold integration
glint calucalation

Heterodyne efficiency, ϵ

Range (km)

Range (km)

GP03 0639 16

Figure 16. Laser heterodyne maximum detection efficiency computed as a function of
range for (a) a single target glint using the two-fold integral Scheil-model
method and (b) a 1 cm radius target (having a Gaussian intensity distribution)
using the approximate four-fold integral method. Fixed parameters of the
calculation are A = P = 2.5 cm, $f_\varrho = f_r = 25$ cm, and $L_o = 5$ cm.
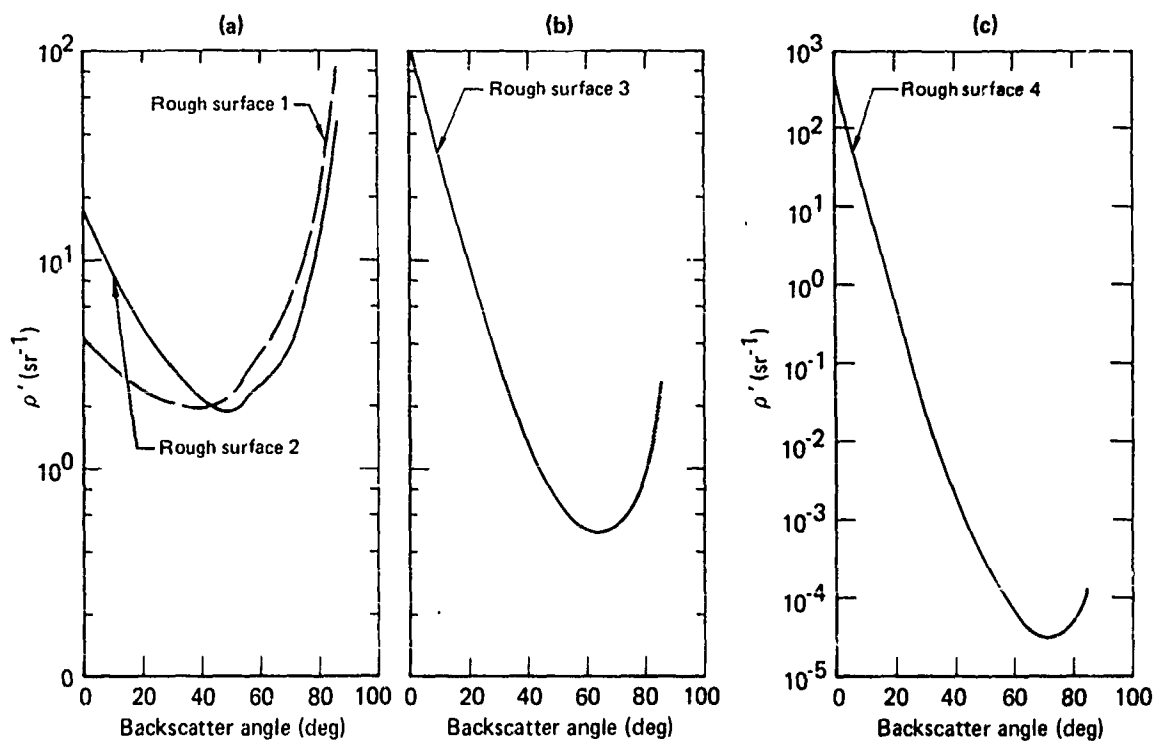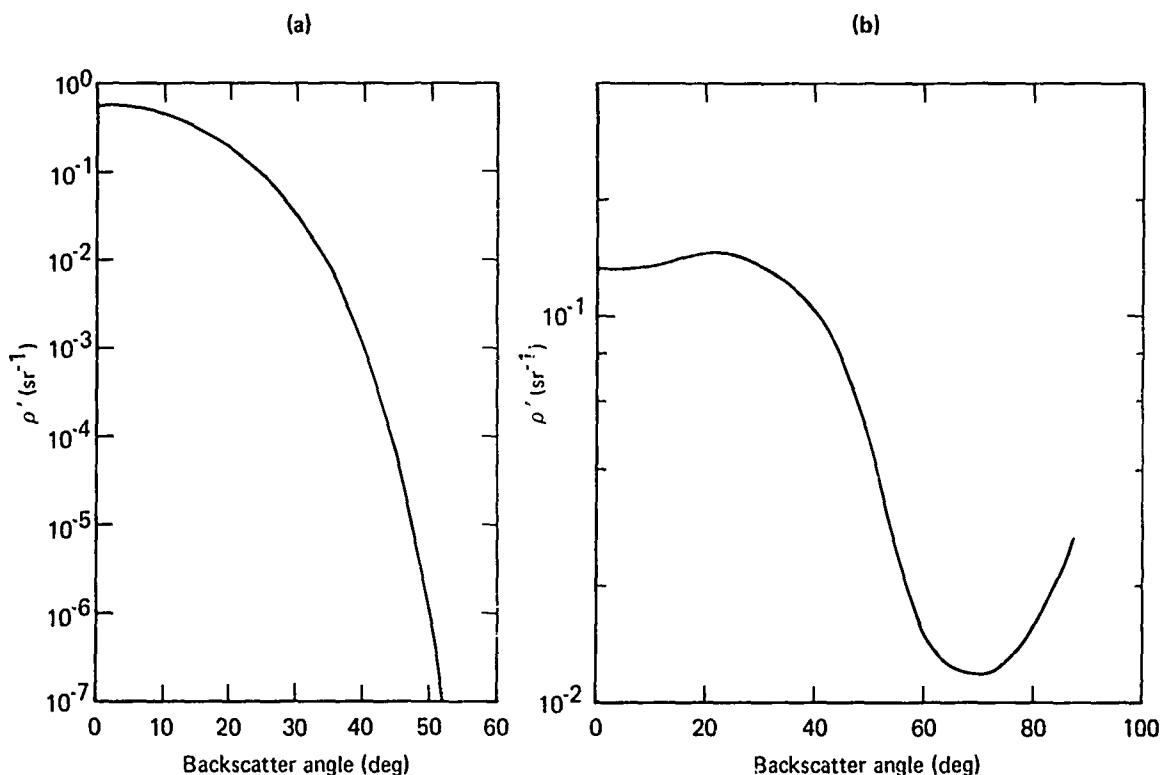
Figure 17. Laser backscatter bidirectional reflectance distribution functions for hypo-
thetical metallic rough surface materials characterized by the ROSSCO
parameters $k\sigma = 3.0$, $s = 0.001$, $m = 1.0$, $n = 100.0$, $\alpha = 0$ and correlation
distances: (a) $k\ell = 1.0$ (rough surface 1), $k\ell = 2.0$ (rough surface 2), (b) $k\ell = 5.0$
(rough surface 3), and (c) $k\ell = 10.0$ (rough surface 4).

50
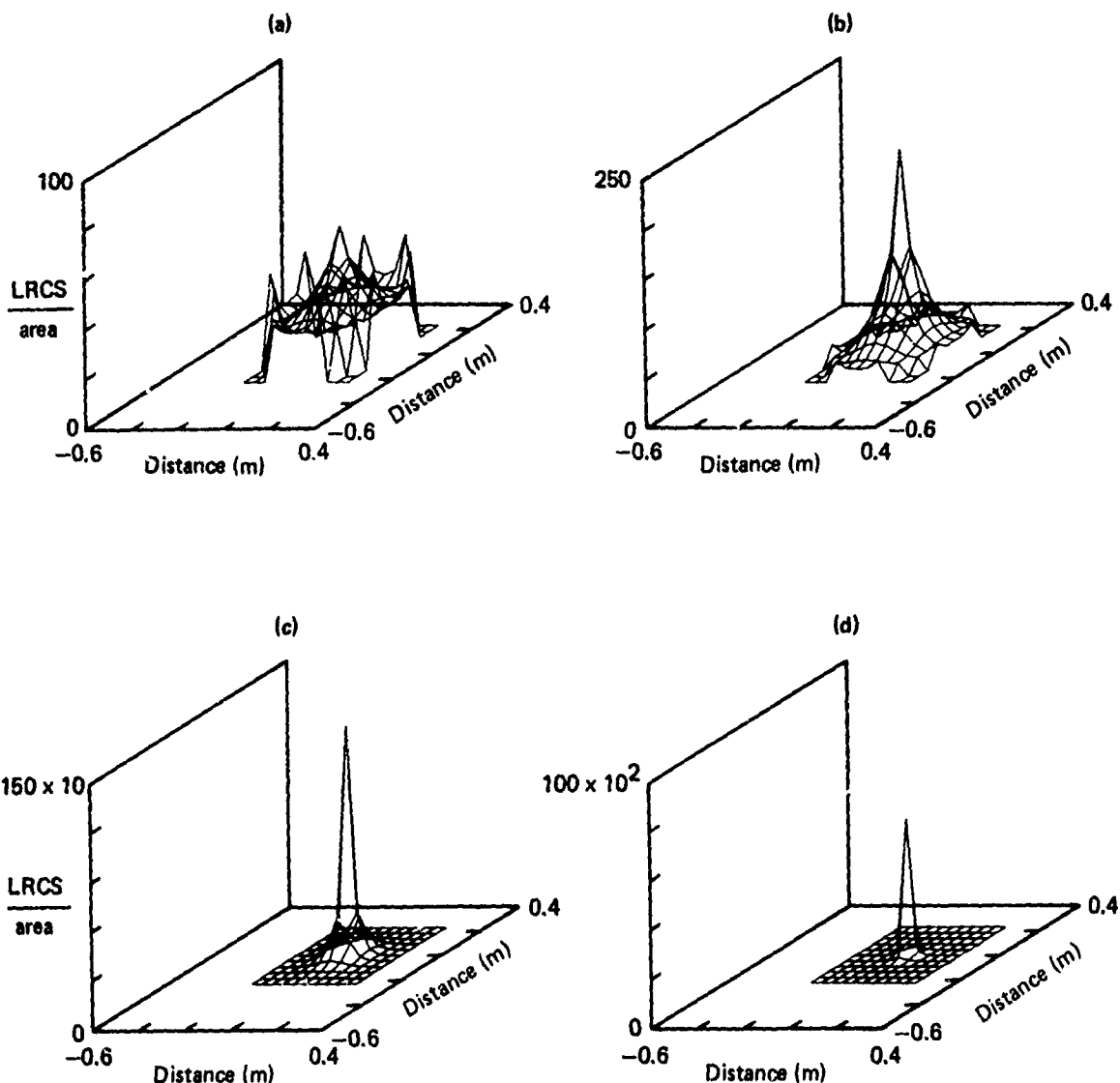
Figure 18. Projected laser cross section per unit area distributions for spherical targets (0.25 m radius) having surface characteristics of (a) rough surface 1, (b) rough surface 2, (c) rough surface 3, and (d) rough surface 4.

To examine the effects of large-scale surface roughness, two different sets of roughness parameters were postulated that result in the Figure 19 ROSSCO predictions of the backscatter laser bidirectional distribution functions. Large-scale surface undulations produce an ensemble of surface glint points for laser reflectance in addition to the diffraction-like scattering from the small-scale roughness. To examine the limiting effects of large-scale roughness, a surface was defined (rough surface A) consisting

51

Figure 19. Laser backscatter bidirectional distribution functions for hypothetical metallic rough surface materials having two scales of roughness characterized by the ROSSCO parameters (a) $k\sigma = 0.0$, $kH = 5.0$, $k\ell = 3.0$, $s = 0.3$, $m = 1.0$, $n = 100.0$, $\alpha = 0$ (rough surface A), and (b) $k\sigma = 0.2$, $kH = 5.0$, $k\ell = 3.0$ $s = 0.6$, $m = 1.0$, $n = 100.0$, and $\alpha = 0$ (rough surface B).

solely of glint points, while a second surface was defined (rough surface B) having a much larger range of surface undulations combined with a small-scale surface roughness. The Figure 19a data show the rapid decrease in the reflectivity of rough surface A with increasing backscatter angle caused by the rapid decrease in the number of glint points. The reflectivity of rough surface B, Figure 19b, contrasts with that of rough surface A because the large surface undulations and small-scale roughness combine to produce an almost constant reflectivity distribution (a Lambertian surface has a constant value of ρ' at all angles). Figure 20 shows the LRCS distribution of spherical targets having surface features parameterized by the ROSSCO parameters of rough surfaces A and B. The principal reflectance from the sphere of rough surface A, Figure 20a, arises from the central distribution of glint points, whereas significant reflectance from the rough surface B sphere, Figure 20b, occurs at locations at the sphere periphery.
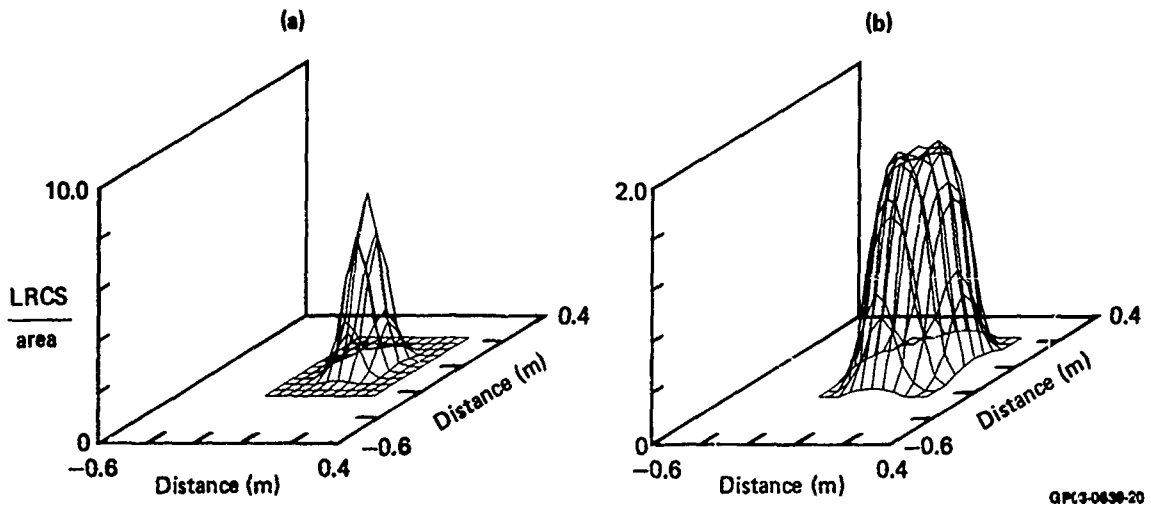
52

Figure 20. Projected laser cross section per unit area distributions for spherical targets (0.25 m radius) having surface characteristics of (a) rough surface A and (b) rough surface B.

To illustrate the effects of surface roughness on the LRCS distribution of conical targets, Figures 21 and 22 provide calculated LRCS/area results, Equations (107)-(114), for cones of rough surfaces A and B at various observation angles. A comparison between the data plotted in Figures 21 and 22 shows the expected result that the principal reflectance contribution from cone A arises from an area near the cone axis (for nonzero observation angles) as a result of the abundance of glint points near the cone axis, whereas the LRCS of cone B is more evenly distributed over the projected outline of the cone as a result of the significant laser scattering produced by rough surface B at angles near grazing incidence. The subsequent section demonstrates the effect of varying LRCS distributions, arising from surface roughness differences, on calculated heterodyne detection efficiencies.
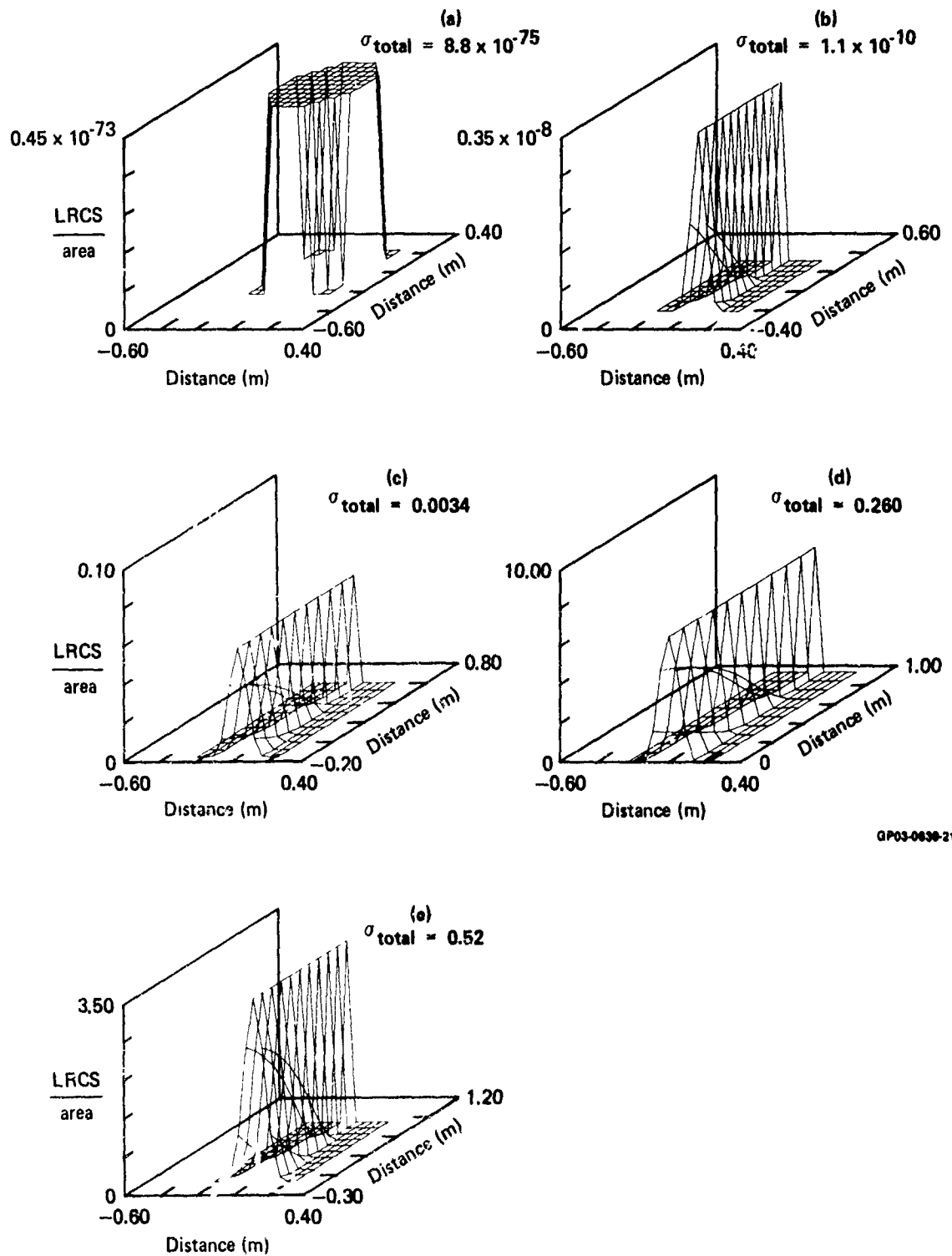
Figure 21. Projected laser cross section per unit area distributions for a conical target having a base radius of 0.25 m, a height of 1.0 m, and a surface finish characterized by rough surface A. Projection direction angles are (a) 0°, (b) 20°, (c) 40°, (d) 60°, and (c) 80°.
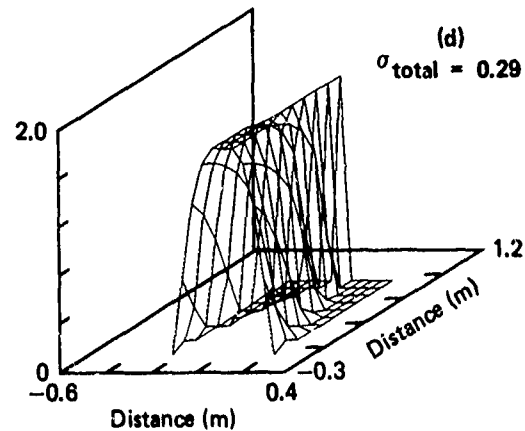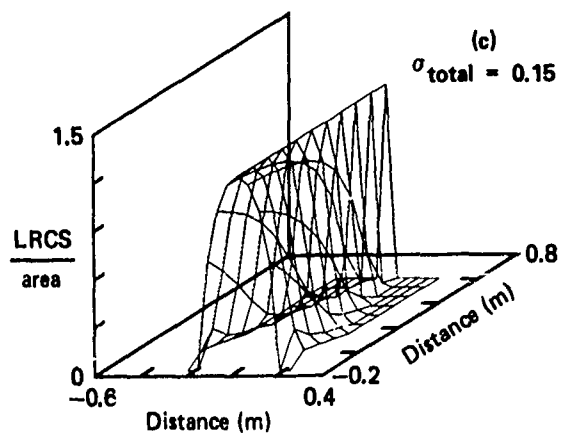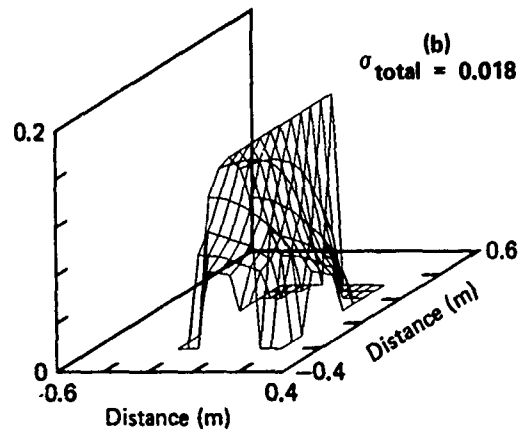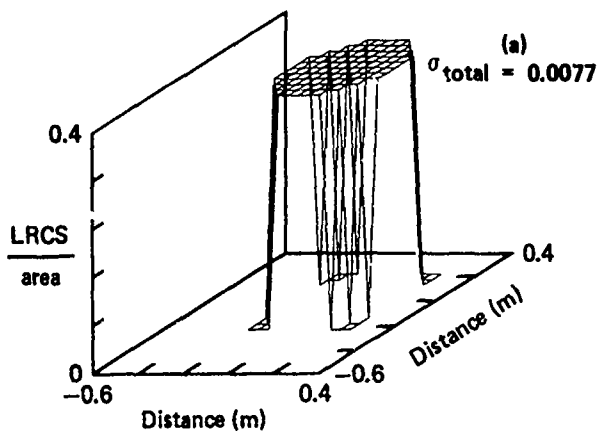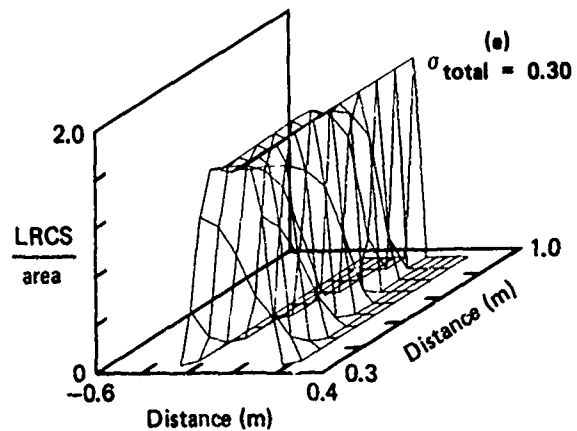
Figure 22. Projected laser cross section per unit area distributions for a conical target having a base radius of 0.25 m, a height of 1.0 m, and a surface finish characterized by rough surface B. Projection direction angles are (a) 0°, (b) 20°, (c) 40°, (d) 60°, and (e) 80°.

GP03-0639-22

55

6.3.4 Efficiency Calculations

A variety of LRCS distributions, such as those depicted in Figures 18, 20, 21, and 22, were used to determine the effects on the calculated heterodyne efficiency of (a) target roughness, (b) target shape, (c) target orientation, and (d) the dimension of the data matrix used in the numerical integration of Equation (67). Calculated values of the heterodyne efficiency for spherical targets having rough surfaces corresponding to rough surfaces 1-4 are tabulated in Table 1 for various dimensions of the variable grid size employed in the numerical outer integration (dummy variable $\vec{\xi}^{+}$) and inner integration (dummy variable $\vec{\xi}^{-}$) of Equation (67). The Table 1 data show (1) a monotonic increase in the calculated heterodyne efficiency with increasing smoothness of the surface and (2) relatively little effect of the calculation grid size on computed results, although the relative error resulting from small grid sizes increases with increasing surface roughness. Both of the trends noted in the Table 1 data are expected from physical and mathematical considerations; however, it is noteworthy that (a) solely surface-roughness effects can account for predicted heterodyne efficiencies differing by an order of magnitude for the same target and (b) computational grid sizes as small as 5x5 can yield efficiency results that are in relatively good agreement with results computed from grid sizes of much higher dimensionality.

TABLE 1. ROUGH SURFACE AND GRID SIZE EFFECTS ON CALCULATED
HETERODYNE EFFICIENCY

Fixed parameters of the calculation are A = P = 2.5 cm, $f_{\ell} = f_{\sigma}$ = 25 cm,
R = 500 m, C_n^2 = 0, sphere radius = 0.25 m

$k\ell$	Rough surface	Grid size				
		5 x 5 (5 x 5)	9 x 9 (9 x 9)	11 x 11 (11 x 11)	5 x 11 (11 x 11)	5 x 11 (5 x 11)
1	1	0.13	0.10	0.11	0.10	0.11
2	2	0.37	0.27	0.27	0.28	0.30
5	3	0.95	0.82	0.74	0.83	0.88
10	4	1.00	1.00	0.95	0.97	1.00

◄── Inner integration
◄── Outer integration

Note Rounded to two significant figures

GP03 0639 26

56

Calculated spherical-target heterodyne efficiencies are tabulated in
Table 2 for various ranges assuming rough-surface textures corresponding to
rough surfaces A and B and a centrally located spherical glint point. The
Table 2 data demonstrate the monotonic increase in the heterodyne efficiency
with increasing range to the target and again illustrate the reduced
heterodyne efficiency resulting from rough surfaces. It is apparent from the
Table 2 data that glint points are relatively more effective in enhancing the
heterodyne efficiency of rough targets vis-a-vis smooth targets.

Calculated conical target heterodyne efficiencies are plotted in Figure
23 as a function of range for rough surfaces 1-4 and in Figures 24-25 as a
function of aspect angle for rough surfaces A and B. The cone efficiency data
plotted in Figures 23-25 substantiate the conclusions drawn from the spherical
target calculations regarding the deleterious effects on the heterodyne
efficiency of roughened surfaces and decreased range. Additionally, however,
the data of Figures 23-25 demonstrate that the aspect angle of three-
dimensional bodies critically influences the heterodyne efficiency because of
the variation in the projected area with aspect angle.

As a final demonstration of the effects of the grid size used in the
numerical calculation of the heterodyne efficiency, Table 3 provides a
comparison of the range-dependent heterodyne efficiencies calculated for a 60°
aspect angle cone of rough surface B for two different grid sizes (11x11 and
21x21). The relatively minor discrepancies observed in the Table 3 data for
the different grid size-calculations indicate that sufficiently precise
efficiency computations can be performed economically for relatively diffuse
scattering targets. Because the major part of the computation time of the
heterodyne efficiency is devoted to the four-fold integral, Equation (67), it
should be expected that the increased running time of the 21x21 grid size of
Table 2 over the 11x11 grid is given by the factor

$$(21/11)^4 = 13.28,$$

which is in good agreement with the actual factor of a 12.6 increase in
running time indicated in Table 3. Thus it is expected that 100 s of
computation on the CDC 6500 (the machine used for the calculations of this
study) are sufficient to perform a heterodyne efficiency computation on a grid

size of 38x38 (both inner and outer integrations) which is sufficient to estimate the heterodyne detection efficiency resulting from a rather complex geometrical shape.

TABLE 2. SPHERICAL TARGET HETERODYNE EFFICIENCIES

- Receiver parameters: $A = P = 25$ cm, $f_\varrho = f_r = 25$ cm, $L_o = 5$ cm
- Target/encounter parameters: radius = 25 cm, $\sigma_\phi = 1$, $C_n^2 = 10^{-14}$ m$^{-2/3}$

| Range (km)	Heterodyne efficiency incoherent/total	
	Rough surface A	Rough surface B
0.5	0.59/0.78	0.18/0.53
1.0	0.87/0.93	0.64/0.74
10.0	0.94/0.96	0.93/0.95

GP03-0639-27

TABLE 3. GRID SIZE EFFECT ON CALCULATED LASER DETECTION HETERODYNE EFFICIENCIES FOR A CONICAL TARGET

Fixed parameters of the calculation are $A = P = 2.5$ cm, $f_\varrho = f_r = 25$ cm, $L_o = 5$ cm, $C_n^2 = 10^{-14}$ m$^{-2/3}$, and $60°$ projection angle for a cone having a surface finish characterized by rough surface B.

Grid size	LRCS	Heterodyne efficiency				Run time (s)
		Range (km)				
		0.5	1.0	5.0	10.0	
11 x 11	0.291	0.0364	0.0719	0.695	0.915	0.71
21 x 21	0.285	0.0317	0.0650	0.688	0.907	8.96
% Difference	2	15	11	1	1	—

GP03-0639 28

58
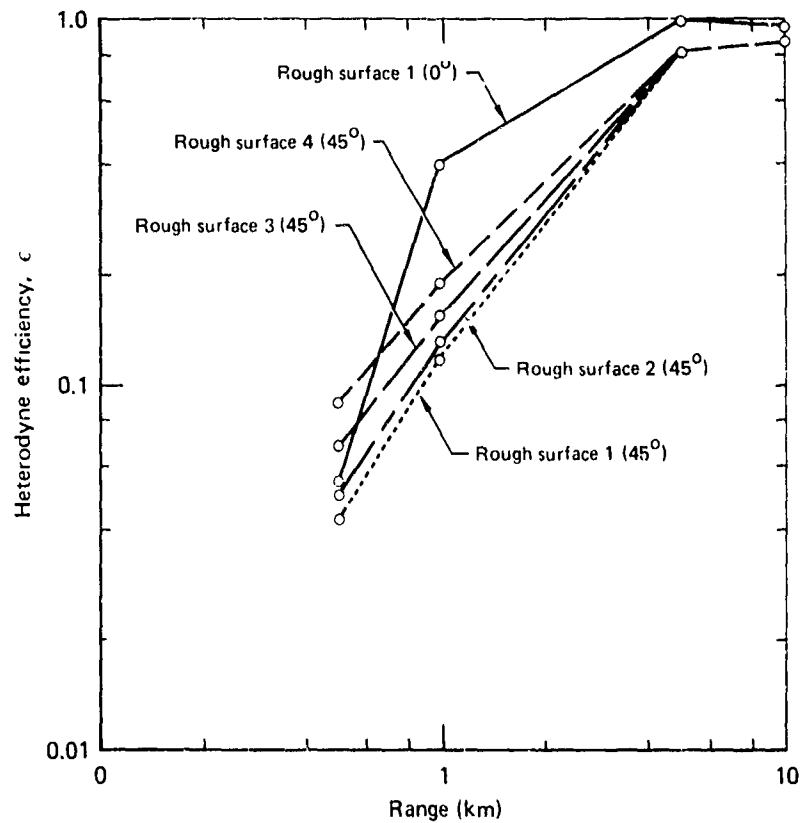
GP03 0639 23

Figure 23. Laser heterodyne maximum detection efficiency values computed as a function of range for conical targets having a base radius of 0.25 m, a height of 1.0 m, and the annotated surface finish characteristics and projection angles. Fixed parameters of the calculation are $A = P = 2.5$ cm, $f_\ell = f_r = 25$ cm, $L_o = 5$ cm, and $C_n{}^2 = 10^{-14}$ m$^{-2/3}$.

Figure 24. Laser heterodyne detection efficiency values computed as a function of viewing (projection) angle for a conical target having a base radius of 0 25 m, a height of 1.0 m, and a surface finish characterized by rough surface A. Fixed parameters of the calculation are $A = P = 2.5$ cm, $f_\ell = f_r = 25$ cm, $L_o = 5$ cm, $C_n^2 = 10^{-14} m^{-2/3}$, and range (R) values are annotated.
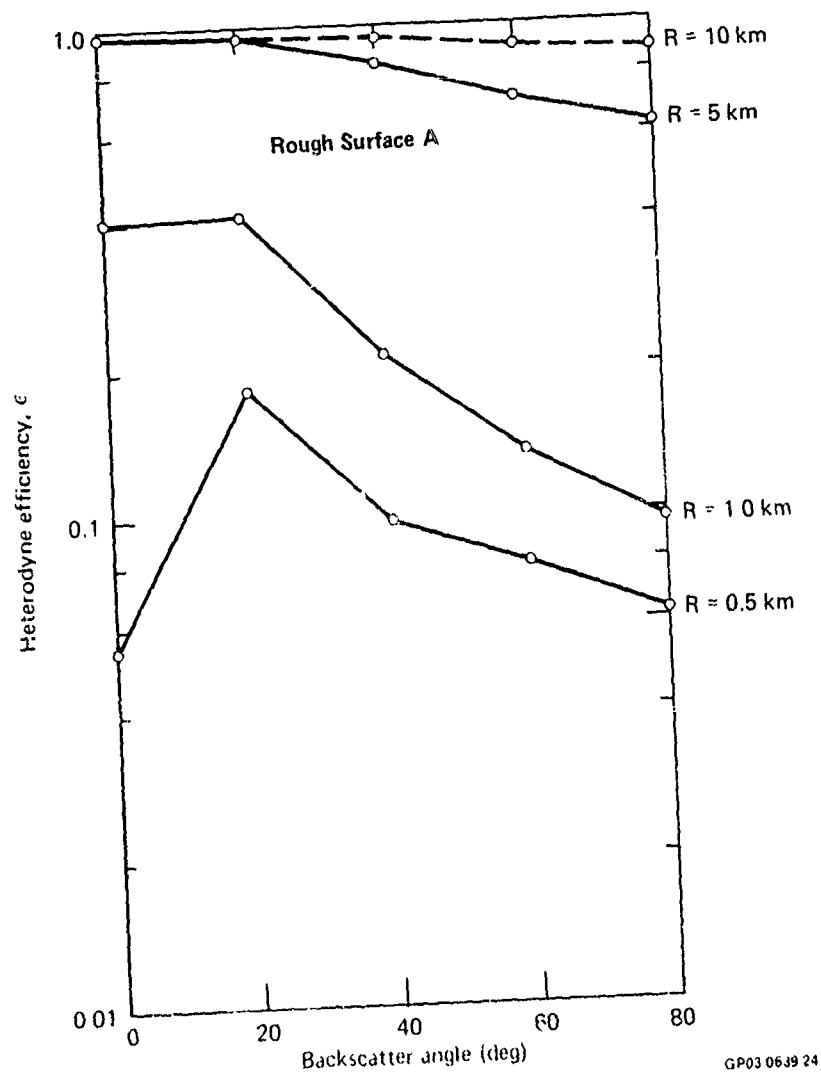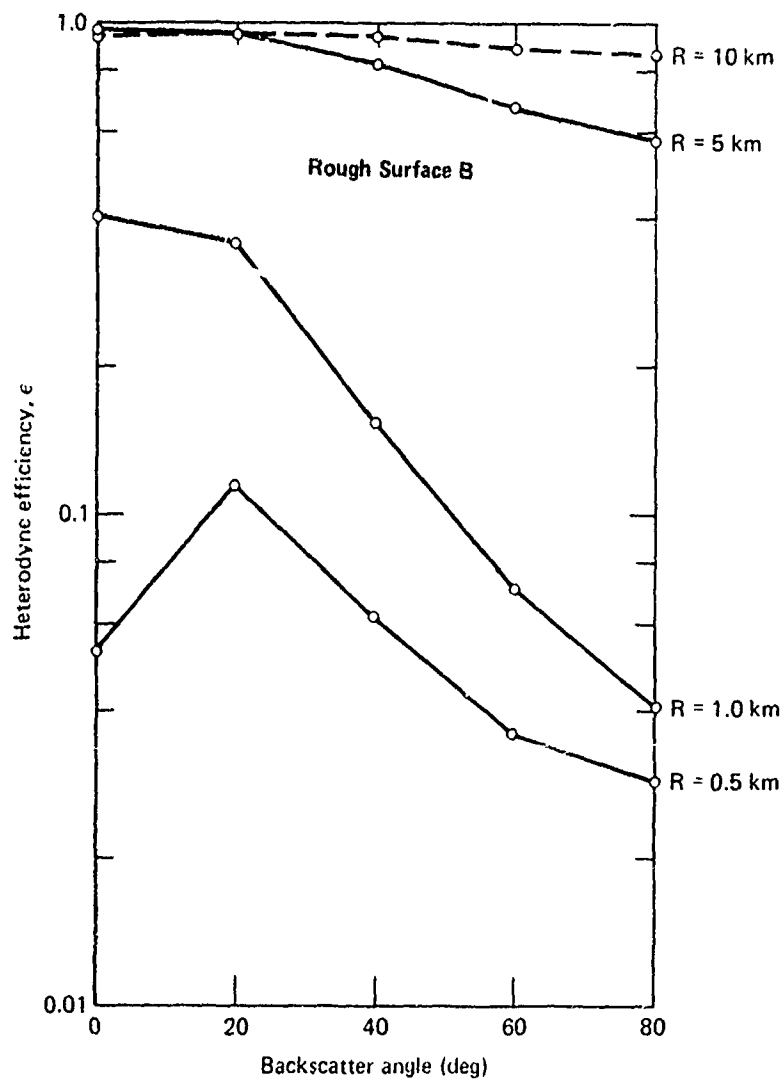
60

Figure 25. Laser heterodyne detection efficiency values computed as a function of viewing (projection) angle for a conical target having a base radius of 0.25 m, a height of 1.0 m, and a surface finish characterized by rough surface B. Fixed parameters of the calculation are A = P = 2.5 cm, f_ϱ = f_r = 25 cm, L_o = 5 cm, $C_n^2 = 10^{-14}$ m$^{-2/3}$, and range (R) values are annotated.

61

REFERENCES

1. J. C. Leader, Bandpass Filtering of Moving-Object Laser Heterodyne Signals by Finite Apertures, Appl. Opt. 17, 1194 (1978).

2. J. C. Leader, Beam Properties of Partially Coherent Curved Beam Waves in the Turbulent Atmosphere, J. Opt. Soc. Am., June 1980.

3. M. Born and E. Wolf, Principles of Optics (Pergamon Press, New York, 1965) Appendix III, pp. 753-754.

4. J. C. Leader, An Analysis of the Frequency Spectrum of Laser Light Scattered from Mov .g Rough Objects, J. Opt. Soc. Am. 67, 109 (1977).

5. J. C. Leader, Far-Zone Range Criteria For Quasi-Homogeneous Partially Coherent Sources, J. Opt. Soc. Am. 68, 1332 (1978).

6. J. C. Leader, Atmospheric Propagation of Partially Coherent Radiation, J. Opt. Soc. Am. 68, 195 (1978).

7. J. C. Leader, Analysis and Prediction of Laser Scattering from Rough Surface Materials, J. Opt. Soc. Am. 69, 610 (1979).

8. J. C. Leader, Intensity Fluctuations Resulting from Partially Coherent Light Propagating though Atmospheric Turbulence, J. Opt. Soc. Am. 69, 73 (1979).

9. D. Fink, Coherent Detection Signal-to-Noise, Appl. Opt. 14, 689 (1975).

10. L. Mandel and E. Wolf, Optimum Conditions for Heterodyne Detection of Light, J. Opt. Soc. Am. 65, 413 (1975).

11. J. M. Bennett, Measurement of the rms Roughness, Autocovariance Function and Other Statistical Properties of Optical Surfaces Using a FECO Scanning Interferometer, Appl. Opt. 15, 2705 (1976).

APPENDIX A: STATIONARY-PHASE EVALUATION OF THE FILTER FUNCTION

The convolution theorem of Fourier transformation can be used to write the filter function [Equation (63)] in the form

$$\tilde{F}(\vec{\mu}') = \frac{R_m^2}{\tilde{\beta}} \iint\limits_{-\infty}^{\infty} d^2\vec{\mu}'' \; \frac{J_1(\mu'' R_m)}{\mu'' R_m} \; e^{-|\mu'-\mu''|^2/2\beta_r} \tag{A1}$$

which becomes

$$\tilde{F}(\vec{\mu}') = \frac{e^{\frac{1}{2}\mu'^2/\tilde{\beta}}}{\tilde{\beta}} \iint\limits_{-\infty}^{\infty} d^2\vec{\rho} \; \frac{J_1(|\vec{\rho}|)}{|\vec{\rho}|} \; e^{-\left(\tilde{\beta} R_m^2\right)^{-1} \left[\frac{1}{2}\vec{\rho}^2 - R_m\vec{\mu}'\cdot\vec{\rho}\right]} \tag{A2}$$

upon introducing the variable change

$$\vec{\rho} = \vec{\mu}'' R_m. \tag{A3}$$

Assuming that

$$\frac{\mu'}{\tilde{\beta} R_m} \gg 1 , \tag{A4}$$

the integral of Equation (A2) can be approximated by the method of double-stationary phase[3] because the complex exponential term in the integrand dominates. The stationary phase point, $\vec{\rho}_o$, is located at

$$\vec{\rho}_o = R_m \vec{\mu}'. \tag{A5}$$

The double-stationary-phase integral formula yields

$$\widetilde{F}(\mu') \cong \widetilde{F}_{sp}(\mu') = 2\pi \, R_m^2 \, \frac{J_1(\mu' \, R_m)}{\mu' \, R_m},$$

(A6)

providing Equation (A4) holds.

APPENDIX B: SERIES EXPANSION EVALUATION OF THE FILTER FUNCTION

Because the Heaviside function can be written in integral form as

$$\theta(x) = \lim_{\epsilon \to 0} \frac{1}{2\pi} \int_{-\infty}^{\infty} \frac{d\tau\, e^{i\tau x}}{(\epsilon + i\tau)} \quad , \tag{B1}$$

the filter function [Equation (63)] can be written as

$$\tilde{F}(\mu') = \lim_{\epsilon \to 0} \frac{1}{2\pi} \iiiint_{-\infty}^{\infty} \frac{d^2\xi^-\, d\tau}{(\epsilon + i\tau)} e^{i\tau(R_m^2 - \xi^{-2})} e^{-\frac{1}{2}\tilde{\beta}\xi^{-2} - i\vec{\mu}' \cdot \vec{\xi}^-} \tag{B2}$$

or

$$\tilde{F}(\mu') = \lim_{\epsilon \to 0} \int_{-\infty}^{\infty} d\tau\, (\tau - i\epsilon)^{-1} (2\tau - i\tilde{\beta})^{-1} e^{i\tau R_m^2} e^{\frac{1}{2} i\mu'^2 (2\tau - i\tilde{\beta})^{-1}} \tag{B3}$$

after integrating over the variable ξ^-. A contour in the complex τ plane bounded by the real axis, and an infinite arc in the upper half plane can be used to perform a contour integration of Equation (B3). This contour encloses a simple pole at $\tau = i\epsilon$, and a combination pole and essential singularity at $\tau = i\tilde{\beta}/2$. The contribution of the pole and essential singularity combination is evaluated by noting that

$$\oint dz \, \frac{f(z)e^{A/(z-z')}}{z - z'} = 2\pi i \sum_{n=0}^{\infty} A^n \, \frac{f^{(n)}(z')}{(n!)^2} \tag{B4}$$

for any analytic function $f(z)$. Equation (B4) follows from the Cauchy integral theorem upon expanding the exponential and integrating term by term using the contour integral method. Also noting that

$$F(z' + A) = \sum_{n=0}^{\infty} A^n \, \frac{f^{(n)}(z')}{n!} \, , \tag{B5}$$

it is clear that

$$\oint dz \, \frac{f(z)e^{A/(z-z')}}{z - z} \approx 2\pi i \, f(z' + A) \, , \tag{B6}$$

providing

$$\frac{A}{z'} \ll 1. \tag{B7}$$

Thus, utilizing the Equation (B6) aproximation to evaluate the combination pole and essential singularity contribution to the contour integration of Equation (B3), the approximate result is

$$\widetilde{F}(\vec{\mu}') \cong \widetilde{F}_E(\mu') = 2\pi \left[e^{-\frac{1}{2}\mu'^2/\tilde{\beta}} (\tilde{\beta})^{-1} - e^{-\frac{1}{2}R_m^2 (\tilde{\beta}+\frac{1}{2}\mu'^2)} (\tilde{\beta} + \frac{1}{2}\mu'^2)^{-1} \right],$$

$$\tag{B8}$$

providing

$$\frac{1}{2} \mu'^2 \ll \tilde{\beta}. \tag{B9}$$